

Coupled Rigid-Block Analysis: Stability-Aware Design of Complex Discrete-Element Assemblies

Gene Ting-Chun Kao^{a,*}, Antonino Iannuzzo^a, Bernhard Thomaszewski^b, Stelian Coros^b, Tom Van Mele^a, Philippe Block^a

^a Block Research Group (BRG), Institute of Technology in Architecture, ETH Zurich, Switzerland

^b Computational Robotics Lab (CRL), Department of Computer Science, ETH Zurich, Switzerland

ARTICLE INFO

Article history:

Received 2 September 2021

Received in revised form 19 November 2021

Accepted 19 January 2022

Keywords:

3D assembly

Computational fabrication

Stability-aware design

Concave shapes

Friction

Contact mechanics

ABSTRACT

The rigid-block equilibrium (RBE) method uses a penalty formulation to measure structural infeasibility or to guide the design of stable discrete-element assemblies from unstable geometry. However, RBE is a purely force-based formulation, and it incorrectly describes stability when complex interface geometries are involved. To overcome this issue, this paper introduces the coupled rigid-block analysis (CRA) method, a more robust approach building upon RBE's strengths. The CRA method combines equilibrium and kinematics in a penalty formulation in a nonlinear programming problem. An extensive benchmark campaign is used to show how CRA enables accurate modelling of complex three-dimensional discrete-element assemblies formed by rigid blocks. In addition, an interactive stability-aware design process to guide user design towards structurally-sound assemblies is proposed. Finally, the potential of our method for real-world problems are demonstrated by designing complex and scaffolding-free physical models.

© 2022 The Author(s). Published by Elsevier Ltd. This is an open access article under the CC BY-NC-ND license (<http://creativecommons.org/licenses/by-nc-nd/4.0/>).

1. Introduction

Discrete-element assemblies are structures formed by individual rigid units without glue or other joinery. The dimension of these assemblies can range from small products to buildings. In architectural contexts, designing such discrete-element assemblies that can stand under their self-weights has many applications. For example, the unit size can be relatively small in some masonry structures but large in prefabricated housing, as shown in Fig. 1. Besides architecture, assessing the stability of discrete-element assemblies can be used in designing furniture, 3D puzzles, toys, or even robotic assembly planning.

Although recent advances in fabrication and construction technologies, such as large-scale additive manufacturing and robotic fabrication, have created new opportunities to design, fabricate, and assemble customised architectural units with complex geometries, a proper tool to design discretised thin structures is lacking and assessing stability during the assembly process remains a difficult task (see Fig. 1a and c). The main challenge in designing such structurally-sound or scaffolding-free discrete-element assemblies is to interactively assess their stability at each

design iteration and the modifications needed to redirect the initial design. Unfortunately, quick interactive tools are rarely used in engineering practice due to insufficient accuracy, while more accurate engineering software suffers from heavy computational effort and complicated parameters tuning.

This paper, therefore, presents a new, fast methodology for an interactive design process that correctly captures the stability of complex discrete-element assemblies. Our method's accuracy is benchmarked against widely used software in engineering practice and demonstrated through physical models.

The study of structural equilibrium and complex assemblies has been a core topic in many research fields, especially in computer graphics, robotics, architecture, and structural mechanics. In what follows, we mainly focus on some research topics relevant to our goal.

The classic Finite Element Method (FEM) is the most commonly used method for analysing structures in many engineering fields. However, much research shows that the standard use of FEM approaches does not provide accurate results when assessing unilateral structures [4–7]. In recent works, FEM methods have been used to assess unilateral assembly modelling each block as a distinct element [8]. Nonetheless, they can only provide a yes-no answer and, thus, cannot be embedded into other optimisation processes such as gradient-based optimisation formulations.

Self-supporting structures are discrete-element assemblies that can stably stand under their self-weight. In particular, much effort has been devoted to exploring freeform self-supporting shapes

* Corresponding author.

E-mail addresses: kao@arch.ethz.ch (G.T.-C. Kao), iannuzzo@arch.ethz.ch (A. Iannuzzo), bthomasz@inf.ethz.ch (B. Thomaszewski), scoros@inf.ethz.ch (S. Coros), vanmele@arch.ethz.ch (T. Van Mele), block@arch.ethz.ch (P. Block).

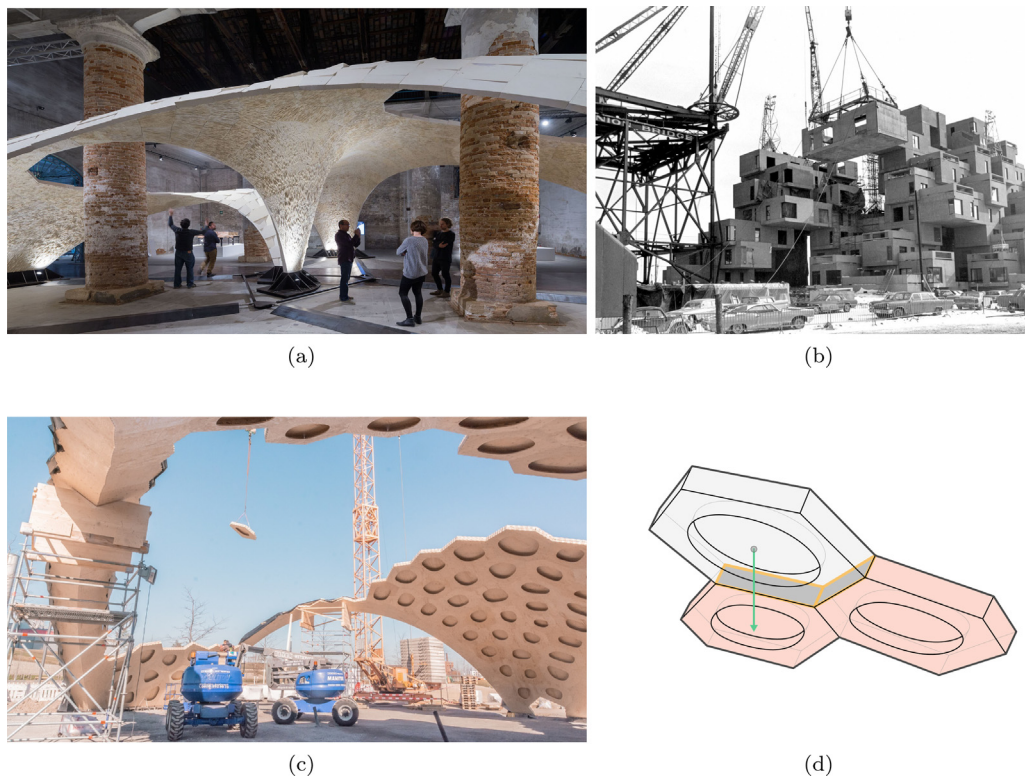


Fig. 1. Architectural design with discrete-element assemblies. (a) Armadillo Vault: a discrete shell structure constructed in stone without any mechanical joints or reinforcements [1]; (b) Prefab modular building construction of Habitat '67 by Safdie Architects [2]; (c) Buga wood pavilion during construction [3]; in (d) a mechanical scheme that can be used to assess the local stability for the Buga wood pavilion (the two pink blocks are assumed fixed). (For interpretation of the references to colour in this figure legend, the reader is referred to the web version of this article.)

such as masonry structures [9–11]. Much research is based on Thrust Network Analysis (TNA), an equilibrium approach developed by Block and Ochsendorf [12]. In the architectural design and fabrication community, RhinoVault, an interactive design tool, has been popular and broadly used for designing funicular structures [13]. However, TNA applies specifically to shell structures. It is not the appropriate tool for designing general discrete-element assemblies.

Physics-based simulations and robot grasp planning have been studied intensively [14–21]. However, most research is devoted to giving a visually convincing rather than a physically accurate result. Contact problems with friction have been recognised as challenging problems [22]. Much research points out that finding an equilibrium solution of unknown contact forces is a necessary but not sufficient condition [23–25], and determining the stability is co-NP complete [18]. Kaufman et al. [26] proposed a staggered algorithm to simulate rigid-body dynamics to realistically model the sliding behaviour using the Maximum Dissipation Principle (MDP) [27]. We, however, are interested in the static analysis as it is easier to steer the structural design. Haas-Heger and Ciocarlie [28] gave good insights into coupling kinematics and static equilibrium problems in the optimisation constraints using MDP. However, their approach is based on Mixed-Integer Programming (MIP) to distinguish between sliding and resting frictions and requires a long computational time and does not apply to general complex assembly problems with many elements.

Masonry structures have been standing for thousands of years, and they were designed and constructed by ancient master builders without the aid of modern engineering methods and technologies. Much research has developed computational methods to understand its structural mechanics. Cundall [29] developed Discrete Element Modelling (DEM) to analyse structures composed of discrete particles for granular materials, which was

later used in the software code for 3DEC [30]. Starting from the work of Lemos [31], it became a popular tool to assess masonry structures or to benchmark new methodologies [5,31–36]. However, DEM solvers require detailed mechanical parameter tunings and a long computational time. Besides, simulating complex concave shapes requires an additional convex decomposition step. In general, historical masonry structures are not modelled using complex block shapes.

Complex assemblies is also a popular research topic and much effort has been paid to designing and creating different types of objects using smaller units, such as toys, furniture, mechanisms, and architectures. Such complex shapes are in some cases designed from a pure geometrical perspective [37–42], while, in other cases, the mechanical stability is also taken into account. Frick et al. [43] introduced a graph-based data structure to handle complex assemblies for stability analysis considering imperfections, but it requires convex decomposition for concave shapes. Yao et al. [44] provided an interactive process to design joinery for furniture and consider structural stability at the same time. However, their analysis result is over-conservative and does not align well with well-accepted analytic or other numerical solutions. Looking at structurally-informed LEGO design, Luo et al. [45] presented a force-based approach that requires physical experiments to tune the optimisation.

Assembly-aware design or stability during assembly is a new research area that has received much attention recently. Kao et al. [46] proposed a design process with a heuristic strategy to assemble discrete shell structures stably without using falsework. They utilised an existing game engine as a stability analysis tool, which is not guaranteed to be reliable. Deuss et al. [11] proposed using a sparse set of tensile chains in replacing dense supports. A more recent study showed the potentiality of using three cooperative robots to achieve scaffold-free construction [47].

The *Rigid-block Equilibrium (RBE)* method was developed by Whiting et al. [48,49], based on the work of Livesley [50,51], who proposed a formulation based on linear programming to analyse the limit load of masonry structures. Whiting et al. [48,49] added a penalty term to Livesley's formulation that measures structural instability such as to enable forward design. RBE has since been successfully applied to a wide range of problems, including forward-design tools and shape optimisation [11,52–60]. In particular, Frick et al. [58] proposed its use for designing discrete-element assemblies in an interactive CAD environment. Shin et al. [7] gave a thorough comparison between RBE and FEM approaches. Wang et al. [52,53] formulated a shape optimisation of topological interlocking for convex assemblies based on an RBE stability analysis without using friction. Kao et al. [54] gave some insights into RBE results from the masonry structure's perspective. After proposing a thorough survey of the state of the art methods, Wang et al. [61] stated that RBE represents one of the best tools in the design process. In general, the RBE approach is preferable over FEM, DEM, or other dynamic simulations because it can more intuitively guide the design from unstable toward stable configurations. RBE's strength is its penalty formulation and the possibility of looking at the internal stress state to understanding the structural response. The penalty formulation provides the users with the localisation of unstable regions instead of only collapse mechanisms that cannot give meaningful structural hints for complex structures. Therefore, it enables different structural design options, such as changing discretisation or connection design (i.e. geometry, shape or using rebar). Although RBE is widely used to design stable assemblies, it suffers from its limitations when friction is involved. We will address RBE's limitation in Section 2.2.

Our research contributions are summarised as follows. Firstly, we recognise and overcome issues of the state-of-the-art RBE implementation. To have an accurate tool for designing structurally informed assemblies with complex shapes and interfaces, we propose a new mathematical formulation that allows for the correct assessment of complex assemblies and excludes RBE's *physically unrealisable* solutions. Our numerical results are accurate and align well with analytical (whenever these are available or possible) and engineering software solutions. Secondly, we demonstrate that our approach is flexible and can be used beyond simple convex shapes. Specifically, we extend an existing graph-based data structure to handle information for complex discrete-element assemblies with concave shapes. This extension is easy to use and does not require any convex decomposition step. Thirdly, our approach is explicit and does not need complicated parameter tuning, which is critical when detailed information about material properties and their translation into numerical parameters is not available. Additionally, it is worth mentioning that our method is *static* and does not require simulating the movement of the objects, such that there is no additional time parameter to tune. Fifthly, we extend our optimisation with a penalty formulation, which enables the formulation to go beyond non-feasible solutions and provides meaningful information about which part of the assembly is not in equilibrium, as in Whiting et al. [48,49]. Lastly, our formulation can be easily integrated into an interactive design workflow to help designers understand structural stability on the global, local scale and find the stable assembly sequence during the early design phase.

2. Theoretical background

To provide the reader with a sufficient amount of information to go through our method, we briefly illustrate the state-of-the-art Rigid-Block Equilibrium (RBE) method and the used assembly data structure. After that, we address what RBE is missing conceptually through three simple 2D examples.

2.1. Rigid-Block Equilibrium (RBE) method and Assembly Data Structure

The RBE method is based on the seminal contributions of Livesley [50,51]. The unilateral contact among blocks is modelled through compressive forces occurring on the interface vertices. In Fig. 2, an assembly \mathcal{A} is composed of a finite set of blocks \mathcal{B} and contact interfaces \mathcal{C} . Each block is a compact closed subset of \mathbb{R}^3 whose boundary is defined as the union of finite planar polygons. The interface C_{jk} between the block j and k is defined as the intersection of \mathcal{B}_j and \mathcal{B}_k , and it is a compact polygonal subset of \mathbb{R}^2 . Therefore, for an assembly \mathcal{A} with l blocks $\mathcal{B} = \{\mathcal{B}_j \mid j \in \{1, \dots, l\}\}$, the set of all interfaces is: $\mathcal{C} = \{C_{jk} = (\mathcal{B}_j \cap \mathcal{B}_k) \mid \exists j, k \in \{1, \dots, l\}, \text{ with } j \neq k \wedge C_{jk} \neq \emptyset\}$. Let m_{jk} be the total number of vertices \mathbf{c}_{jk}^i of the interface C_{jk} with $i \in \{1, \dots, m_{jk}\}$. $(\hat{\mathbf{u}}_{jk}, \hat{\mathbf{v}}_{jk}, \hat{\mathbf{n}}_{jk})$ denotes the unit basis vector representing the local reference system of the planar interface C_{jk} where $\hat{\mathbf{n}}_{jk}$ is the unit normal vector pointing towards the block \mathcal{B}_k . Note that although C_{jk} and C_{kj} denote the same interface, the corresponding reference systems are not the same. The unknown reaction force $\mathbf{f}_{jk}^i \in \mathbb{R}^3$ acting on the vertex \mathbf{c}_{jk}^i can be decomposed into three components $f_{jkn}^i \hat{\mathbf{n}}_{jk}$, $f_{jku}^i \hat{\mathbf{u}}_{jk}$, and $f_{jkv}^i \hat{\mathbf{v}}_{jk}$. The requirement that only compressive forces are admitted is modelled as a non-negativity constraint on the normal force component:

$$f_{jkn}^i \geq 0, \quad \forall i, j, k. \quad (1)$$

For simplicity, we use bold symbol $\mathbf{f}_{jkn}^i \in \mathbb{R}^3$ to represent $f_{jkn}^i \hat{\mathbf{n}}_{jk}$. Similarly, we consider the nodal friction force $\mathbf{f}_{jkt}^i \in \mathbb{R}^3$ combining the two arbitrary, mutually-orthogonal, in-plane shear components $f_{jku}^i \hat{\mathbf{u}}_{jk} + f_{jkv}^i \hat{\mathbf{v}}_{jk}$, where $f_{jku}^i, f_{jkv}^i \in \mathbb{R}$.

To have all blocks in static equilibrium, external forces need to be balanced by all internal unknown net force and torque. In particular, for each block six equilibrium equations have to be written. We can compactly summarise all these equations in a matrix form:

$$\mathbf{A}_{eq} \mathbf{f} = -\mathbf{p}, \quad (2)$$

where the coefficients of the equilibrium equations are collected in the matrix $\mathbf{A}_{eq} \in \mathbb{R}^{6 \cdot l \times 3 \cdot s}$, being $s = \sum_{k=1}^l \sum_{j=1}^l m_{jk}$ the total number of interface corners; $\mathbf{f} \in \mathbb{R}^{3 \cdot s}$ collects all interface unknown forces, and $\mathbf{p} \in \mathbb{R}^{6 \cdot l}$ the external forces lumped on each block's mass centre. We refer the reader to Appendix A for further details.

To have stable assemblies, Eq. (2) is the necessary condition that needs to be satisfied. If we cannot find any solution \mathbf{f} , we can claim that the structure is not stable. Typically, \mathbf{A}_{eq} is not a square matrix because of the structure's indeterminacy, and we have less equations than unknowns; in general, $6 \cdot l < 3 \cdot s$. Therefore, the solution \mathbf{f} is not unique, and it does not necessarily represent the actual force distribution on the interface. For these reasons, optimisation approaches represent a valid strategy to select one of the possible internal stress states.

For unstable assemblies, Eq. (2) does not admit any solution. To extend the solution space and to measure the corresponding infeasibility, Whiting et al. [48,49] allowed for tensile capacity through the introduction of a penalty formulation. Specifically, they decoupled the normal force f_{jkn}^i into its positive f_{jkn}^{i+} and negative f_{jkn}^{i-} parts, such that $\forall i, j, k, f_{jkn}^i = f_{jkn}^{i+} - f_{jkn}^{i-}$, with $f_{jkn}^{i+}, f_{jkn}^{i-} \geq 0$. Therefore, an additional unknown for each vertex was introduced. All the unknowns can be collected in the vector $\tilde{\mathbf{f}} \in \mathbb{R}^{4 \cdot s}$ and the equilibrium of the entire assembly can be written using the same equilibrium matrix in Eq. (2) as:

$$\mathbf{A}_{eq} \mathbf{B} \tilde{\mathbf{f}} = -\mathbf{p}, \quad (3)$$

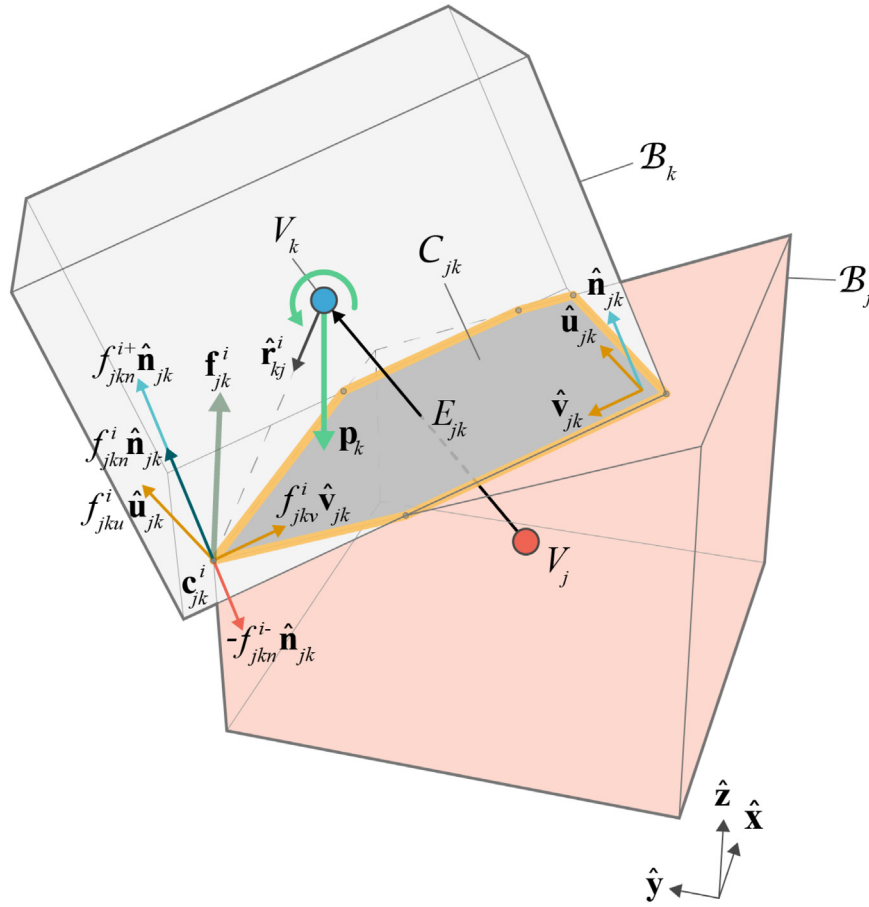


Fig. 2. Notations adopted to describe the equilibrium equations of the assembly. The pink colour represents supports, i.e. fixed blocks, and grey is used to denote free blocks. Assembly data structure is a directed graph $G(V, E)$, where vertex V_j stores information of B_j information while edge E_{jk} stores all interface C_{jk} information. \mathbf{f}_{jk}^i represents the unknown nodal force acting on the vertex i of interface jk : it can be decomposed into three mutually orthogonal vectors using the local reference system of the interface $(\hat{\mathbf{u}}_{jk}, \hat{\mathbf{v}}_{jk}, \hat{\mathbf{n}}_{jk})$. (For interpretation of the references to colour in this figure legend, the reader is referred to the web version of this article.)

where \mathbf{B} is a matrix that maps $\tilde{\mathbf{f}}$ to \mathbf{f} . For more details, we refer the reader to [Appendix A](#).

To model the Mohr–Coulomb friction cone constraint, the friction is bounded by the positive part of the normal force:

$$|f_{jkt}^i| \leq \mu f_{jkn}^{i+}, \quad \forall i, j, k. \quad (4)$$

A standard strategy to speed up the solving process is to linearise the original Mohr–Coulomb friction cone with a given number of planes. The linearised equations have to be written on all interface vertices and can be collected in the following matrix form:

$$\mathbf{A}_{fr} \mathbf{B} \tilde{\mathbf{f}} \leq \mathbf{0}, \quad (5)$$

where \mathbf{A}_{fr} collects all coefficients in a large sparse matrix. For a detailed explanation, we refer the reader to [Appendix B](#).

Combining the equilibrium condition (Eq. (3)) with the linearised friction constraint (Eq. (5)), the entire optimisation problem can be expressed as a quadratic programming (QP) problem:

$$\begin{aligned} \min_{\tilde{\mathbf{f}}} \quad & \frac{1}{2} \tilde{\mathbf{f}}^T \mathbf{H} \tilde{\mathbf{f}} \\ \text{s.t.} \quad & \mathbf{A}_{eq} \mathbf{B} \tilde{\mathbf{f}} = -\mathbf{p} \\ & \mathbf{A}_{fr} \mathbf{B} \tilde{\mathbf{f}} \leq \mathbf{0} \\ & f_{jkn}^{i+}, f_{jkn}^{i-} \geq 0, \quad \forall i, j, k, \end{aligned} \quad (6)$$

where \mathbf{H} is the diagonal square matrix that collects all weights attributed to different force components [49], with the tensile

forces highly penalised. Compared to a linear objective function, the quadratic one returns a linear-elastic force distribution on the interface. For more detailed discussions we refer the reader to the work of Kao et al. [54]. Optimisation problem (6) represents the original RBE formulation as in Whiting et al. [48,49]. It is worth noting that RBE is a strictly force-based approach, without coupling internal stress states with corresponding displacements. As in Whiting et al. [48,49], an assembly is assumed stable if problem (6) returns a solution without tensile forces.

To efficiently handle RBE information, we utilise the assembly data structure proposed in Frick et al. [43]. The assembly data structure is a graph-based data structure where a directed graph $G(V, E)$ is used to represent the entire assembly \mathcal{A} . The vertices V store block geometries information \mathcal{B} , and the directed edges E store all contact information \mathcal{C} . The graph edge is directed. Indeed, although interfaces C_{jk} and C_{kj} collect the same vertices, the unknown forces corresponding to the same corner are reversed for Newton's third law. This shows the reason why the axes of the C_{jk} and C_{kj} local reference system are pointing in the opposite direction. For a more detailed discussion about the assembly data structure, we refer the reader to [Appendices A and B](#).

2.2. Issues of the RBE approach

To show when RBE fails to predict the stability when friction is involved, we illustrate the following two paradigmatic examples, called model H (shown in [44]) and A , in [Fig. 3](#). After that, we

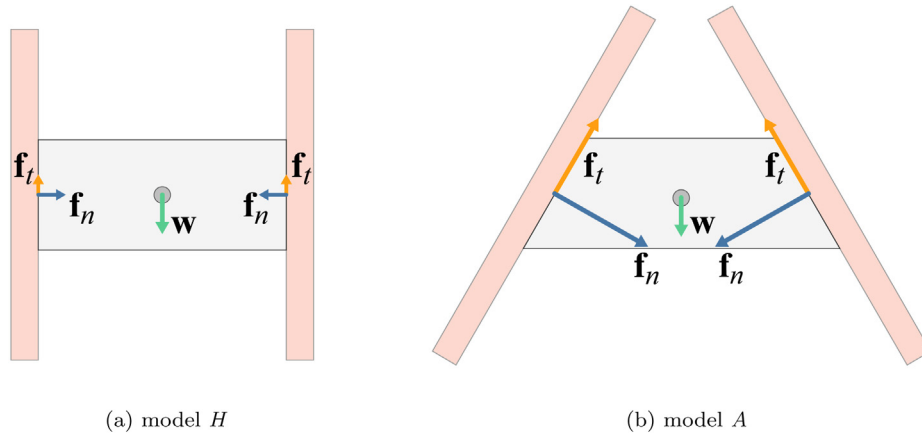


Fig. 3. Two peculiar examples show some of RBE's issues. The free block (grey) is always detected as in equilibrium.

explain how we propose to overcome these issues looking at a simple 2D wedge example, Fig. 4.

For model *H*, we can imagine one free block placed between two parallel fixed walls, which can also represent robot-hand grippers. Regardless of the size of the central block and the friction coefficient, RBE always finds a solution such that the free block is stable. Indeed, to be in static equilibrium, all forces have to cancel out. In the vertical direction, the free block's self-weight \mathbf{w} is balanced by two tangential contact reactions \mathbf{f}_t . In the horizontal direction, RBE finds two normal forces \mathbf{f}_n that cancel each other out. Thus, for any tangential force distribution with any friction coefficient, RBE always finds two large enough normal forces that simultaneously satisfy the Mohr–Coulomb criterion and cancel each other out. In other words, those valid static equilibrium solutions always exist in the constraint solution space defined by Eq. (2). However, if the middle block is not *prestressed*, e.g. due to the robotic grippers, the normal forces should not exist in the real-world scenario. In fact, such a bizarre equilibrium solution is not wrong; it only comes from the original rigid-body assumption that the normal force can occur without any deformation. It is a *physically unrealisable* solution when the free block is *not prestressed*, and generated by a pure force-based optimisation that does not take those considerations into account. In the case of associative behaviour, the solution of the force-based problem is linked to the solution of a dual displacement-based problem as shown in [62,63] for a finite friction capacity, or through an energy-based dualisation for an Heymanian material model in [64,65]. RBE returns a force-based solution that assumes its dual displacement-based solution exists, regardless if it needs prestress or not. A simple way to avoid the *H* model's problem is to couple equilibrium with kinematics and allow for a negligible numerical overlapping; since RBE assumes all blocks to be rigid and non-deformable, having two simultaneous overlaps between supports is impossible.

Comparable to model *H*, the reader can intuitively imagine that in model *A* the free block would fall down if it is rigid and not prestressed. However, if we try to solve this model in the same way used for the *H* model, RBE would still provide the solution shown in Fig. 3b. Therefore, something is still missing; besides the deformation aspect, all reaction forces, particularly tangential forces, have to be compatible with possible rigid-body motions [66], and, all tangential forces are possible only if the corresponding normal forces are activated. With these assumptions, model *A* without prestressing is no longer feasible. In other words, all possible rigid-body motions have to be considered. In model *A*, the only admissible movement is a downward vertical displacement of the central block. Once the contact of one of

the two surfaces is lost, admissible force solutions are no longer possible.

The RBE method is a pure force-based approach and it fails to capture some scenarios as discussed in the *H* and *A* model. The optimiser greedily finds *physically unrealisable* solutions (without prestressing) as long as those solutions satisfy equilibrium and friction cone constraints. In some cases, wrong solutions included in the RBE's solution space can be taken out by looking at the admissible dual movements, but in many other cases it is not possible to simply exclude them from the solution space.

Inspired by Omata and Nagata [67], we observe that not all forces are *physically realisable* concerning rigid-body movements. To be more specific, the reaction forces are *realisable* only if we can find a compatible rigid-body motion. The friction force occurs in the opposite direction of a potential relative movement to prevent the object from sliding such that the acceleration remains zero. Additionally, the normal reaction force is activated only if the two adjacent points are in contact. When there is a detachment, the normal force has to be zero and, consequently, the friction force must be zero as well (bounded by the Mohr–Coulomb criterion).

Fig. 4 shows two possible equilibrated solutions of the wedge model obtained with RBE. Both models share the same geometry and boundary conditions but are inclined at a different angle. In Fig. 4a, we depict a possible rigid-body motion defined by an in-plane rotation and translation, collected in the vector $\delta \mathbf{q}_3$ describing the motion of block \mathcal{B}_3 . The nodal friction forces \mathbf{f}_{13t}^1 and \mathbf{f}_{23t}^1 found by RBE are compatible with nodal displacements \mathbf{d}_{13t}^1 and \mathbf{d}_{23t}^1 . Similarly, if a contact point tends to detach, the nodal normal force cannot be activated. Indeed, no reaction force can occur on the vertex \mathbf{c}_{23}^2 because of the relative detachment \mathbf{d}_{23n}^2 .

Conversely, Fig. 4b illustrates how an admissible equilibrated solution is not compatible with a potential rigid-body motion. The contact forces obtained using RBE are in equilibrium as they balance the block's self-weight. However, these forces are not compatible with a pure translation of the block \mathcal{B}_3 . Indeed, contact forces \mathbf{f}_{23n}^1 and \mathbf{f}_{23t}^1 are not compatible because of the normal detachment \mathbf{d}_{23n}^1 . Additionally, this equilibrated solution is not compatible with the rigid-body motion depicted in Fig. 4a, as \mathbf{f}_{13n}^2 and \mathbf{f}_{13t}^2 are not admissible because of the dual detachment.

Importantly, in the present paper, all friction forces are *static*, while *infinitesimal* rigid-body motions represent *virtual* displacements. The aim is to couple internal forces with *infinitesimal* rigid-body motion in order to discard equilibrated solutions that are not compatible with any rigid-body motion, and in this sense, not *realisable*.

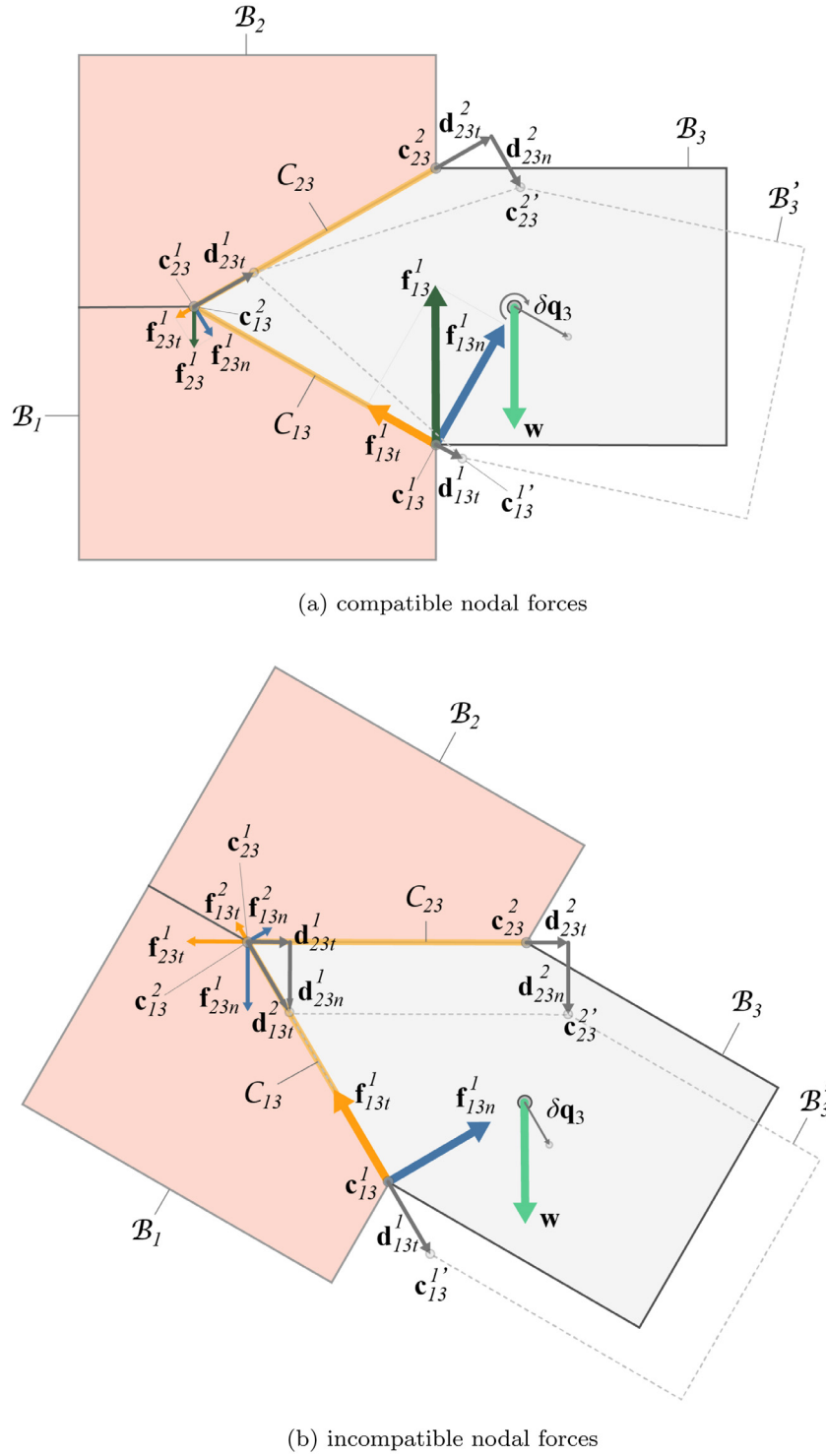


Fig. 4. Model wedge: nodal forces have to be compatible with virtual rigid-body motion; otherwise, those nodal forces are not physically *realisable*.

The physical limitations highlighted on the H , A , and *wedge* models can frequently appear in 3D assemblies, and they are intrinsic in geometries with non-planar interfaces. Indeed, in Fig. 1d, the interface between free and fixed blocks is non-planar, and, upon closer inspection the reader can see a parallelism with model A. Even though the RBE provides proper solutions in some cases, e.g. an arch subjected to in-plane loads (see Fig. 6), we cannot determine in advance if treating a specific problem with a pure force-based approach is sufficient. In the worst case, when RBE fails, it falsely claims a non-prestressed

and unstable structure is safe, leading to wrong design choices or assessment strategies. Thus, a procedure that correctly accounts for these aspects is needed. This paper aims to tackle these aspects through a nonlinear constrained optimisation problem to discard *unrealisable* solutions and provide an accurate approach for discrete-element assembly analysis. We call this approach the Coupled Rigid-Block Analysis (CRA) method as it combines the original equilibrium formulation of RBE with kinematics. In Section 3, this new numerical formulation will be introduced and discussed.

3. Coupled Rigid-Block Analysis (CRA) method

In Section 3.1, to introduce the CRA method, we first formulate the pure force-based optimisation problem and then we couple it with the kinematics through specific additional constraints. After that, we introduce the penalty formulation to measure unstable structures (Section 3.2). The penalty formulation represents the extended version of the original RBE method proposed by Whiting et al. [48,49]. Lastly, in Section 3.3, we extend the data structure used by Frick et al. [43] to account for complex assemblies.

3.1. Problem formulation

The force-based formulation that we start from is:

$$\min_{\mathbf{f}} \|\mathbf{f}_n\|_2^2 \quad (7a)$$

$$\text{s.t. } \mathbf{A}_{eq} \mathbf{f} = -\mathbf{p} \quad (7b)$$

$$\mathbf{A}_{fr} \mathbf{f} \leq \mathbf{0} \quad (7c)$$

$$f_{jkn}^i \geq 0, \quad \forall i, j, k, \quad (7d)$$

where Eq. (7b) enforces the equilibrium only using compressive forces (Eq. (7d)) and Eq. (7c) the Mohr-Coulomb material failure criterion. The objective function represents the squared norm of all contact forces based on Gauss's principle of least constraint [68]. Nonetheless, as proved in Mattikalli et al. [18] and Pang and Trinkle [24], the equilibrium alone does not represent a sufficient condition for the stability. To impose the compatibility between forces and rigid-body motion, we consider *virtual* displacements. In particular, the first aspect is to define the space of all possible *infinitesimal* admissible rigid-body displacements. We denote with $\delta \mathbf{q}_k \in \mathbb{R}^6$ the virtual displacement vector of B_k , where the first three components of $\delta \mathbf{q}_k$ are rigid translations $[\delta q_{k,x} \ \delta q_{k,y} \ \delta q_{k,z}]^T$ and the last three the rigid rotations $[\delta q_{k,rx} \ \delta q_{k,ry} \ \delta q_{k,rz}]^T$. The piecewise rigid displacement field describing the motion of the entire assembly is a function of the Lagrangian parameters collected in the vector $\delta \mathbf{q} \in \mathbb{R}^{6 \cdot I}$.

Based on the well-known duality relation for rigid bodies, the kinematic matrix can be expressed as the transpose of the equilibrium matrix $\mathbf{A}_{eq}^T \in \mathbb{R}^{3 \cdot s \times 6 \cdot I}$ [69]. Therefore, the relative displacement $\delta \mathbf{d} \in \mathbb{R}^{3 \cdot s}$ of the vertices can be expressed through the following relation:

$$\mathbf{A}_{eq}^T \delta \mathbf{q} = \delta \mathbf{d}. \quad (8)$$

Similar to the nodal force \mathbf{f}_{jk}^i , the relative *virtual* displacement $\delta \mathbf{d}_{jk}^i \in \mathbb{R}^3$ of the vertex \mathbf{c}_{jk}^i and it can be decomposed into three components $\delta \mathbf{d}_{jkn}^i$, $\delta \mathbf{d}_{jkt}^i$, and $\delta \mathbf{d}_{jku}^i$, with $\delta \mathbf{d}_{jkn}^i$ the relative normal displacement, $\delta \mathbf{d}_{jkt}^i$ the relative tangential sliding displacement. Afterwards, we introduce two nonlinear constraints to exclude *physically unrealisable* forces.

Firstly, we need to enforce the compatibility between forces and rigid-body motion in two directions, tangential sliding and normal detachment. For a potential sliding motion, we enforce the alignment among friction forces and corresponding virtual sliding movements using the following nonlinear constraints for each contact \mathbf{c}_{jk}^i :

$$\mathbf{f}_{jkt}^i = -\alpha_{jk}^i \delta \mathbf{d}_{jkt}^i, \quad \alpha_{jk}^i \geq 0, \quad \forall i, j, k, \quad (9)$$

where α_{jk}^i is a non-negative scalar used to relate the friction force \mathbf{f}_{jkt}^i direction with the relative sliding displacement $\delta \mathbf{d}_{jkt}^i$. Note that friction and virtual sliding movements are aligned but pointing towards opposite directions. Also, when the virtual sliding

movement is zero, the friction force is zero as well. From a physical perspective, constraint (9) ensures only that the direction of the friction force has to be compatible with the corresponding relative virtual tangential displacement. The need for such a requirement was also pointed out in Omata and Nagata [67], which stated that enforcing a static friction force to the opposite sliding direction restricts the force solution space properly, as also shown in Fig. 4.

Secondly, the compatibility among normal forces and corresponding relative displacements has to be enforced. In other words, we need to ensure normal forces appear only if two blocks are in contact; otherwise, when detachment happens, they have to be zero. We model this behaviour as a complementarity constraint:

$$\begin{aligned} f_{jkn}^i (\delta d_{jkn}^i + \varepsilon) &= 0, \\ f_{jkn}^i, (\delta d_{jkn}^i + \varepsilon), \varepsilon &\geq 0, \quad \forall i, j, k, \end{aligned} \quad (10)$$

where ε is a very small numerical overlapping parameter, i.e. from 10^{-5} to 10^{-4} of the block dimension. The inclusion of ε assures that the normal forces occur only when two blocks slightly overlap.

Finally, combining the original equilibrium formulation (7) with the additional constraints expressed in Eqs. (8)–(10) the new QP formulation with nonlinear constraints is:

$$\begin{aligned} \min_{\mathbf{f}, \delta \mathbf{q}, \alpha} \quad & \|\mathbf{f}_n\|_2^2 + \|\alpha\|_2^2 \\ \text{s.t.} \quad & \mathbf{A}_{eq} \mathbf{f} = -\mathbf{p} \\ & \mathbf{A}_{fr} \mathbf{f} \leq \mathbf{0} \\ & \mathbf{A}_{eq}^T \delta \mathbf{q} = \delta \mathbf{d} \\ & f_{jkn}^i (\delta d_{jkn}^i + \varepsilon) = 0 \\ & \mathbf{f}_{jkt}^i = -\alpha_{jk}^i \delta \mathbf{d}_{jkt}^i \\ & |\delta \mathbf{d}_{jkt}^i| \leq \eta \\ & f_{jkn}^i, \alpha_{jk}^i, (\delta d_{jkn}^i + \varepsilon), \varepsilon, \eta \geq 0, \quad \forall i, j, k. \end{aligned} \quad (11)$$

The objective function here includes the additional term α that collects all α_{jk}^i , and we solve the problem in a least square formulation. For simplicity, we follow the RBE-style formulation to model the linearised friction constraints. Alternatively, those constraints can also be modelled with second-order cone constraints to reduce the computational cost [70,71]. It is worth noting that problem (11) can be thought of as an optimisation problem with equilibrium constraints. Ferris and Tin-Loi proposed a nonlinear programming formulation to define limit states of masonry structure composed of rigid blocks [72]. Several differences between the two formulations can be pointed out: (i) the objective function in (11) minimises the amount of the normal contact forces and does not consider the minimum of the “load factor solutions” as in [72]; (ii) problem (11) explicitly models the alignment between tangential displacements and friction forces, which is key when modelling the mechanics of sharp wedge connections; and, (iii) as will be shown in Section 3.2, formulation (11) represents an ideal base to implement a penalty formulation in order to measure the structural instability. Additionally, although small displacement fields are used, optimisation problem (11) is nonlinear, so each displacement value $\delta \mathbf{d}_{jkt}^i$ is bounded to a small number η (i.e. $10^{-3} - 10^{-2}$ of the block dimension) to avoid local minimum solutions that are far from the initial reference configuration. Note that problem (11) is infeasible when a structure is unstable. The additional constraints combining equilibrium and kinematics reduce the solution space excluding *unrealisable* equilibrated solutions. As we will show, this is reflected in two aspects: (i) it allows for better capturing of the limit states; and (ii) when the structure is in a stable configuration, it

provides more realistic results. As a consequence, it represents a good mathematical base to be used in a penalty formulation. In addition, optimisation (11) implicitly guarantees that the work due to external forces for the corresponding displacements is non-negative:

$$\mathbf{p}^\top \delta \mathbf{q} \geq 0. \quad (12)$$

For a detailed derivation of relation (12), we refer the reader to [Appendix C](#).

3.2. Analysing infeasible structures

In comparison with other approaches, one of the true potentials of the RBE method is that it can analyse unstable structures as illustrated in Section 2.1. As the idea behind our formulation is similar to the RBE approach, we include the penalty formulation in the same qualitative way. We also allow for tensile forces and decouple the normal force \mathbf{f}_{jkn}^+ into its positive \mathbf{f}_{jkn}^+ and negative \mathbf{f}_{jkn}^- parts. Thus, the f_{jkn} in Eq. (10) can be replaced with the positive part of normal force f_{jkn}^+ . Despite the previous RBE formulation, to avoid the simultaneous presence of both negative and positive parts on the same vertex, we introduce the following complementarity constraint:

$$f_{jkn}^+ f_{jkn}^- = 0. \quad (13)$$

As f_{jkn}^+ and f_{jkn}^- cannot coexist, Eq. (4) with constraint (13) implicitly avoids friction when tension force occurs. By adding all penalty forces and additional constraints, optimisation problem (11) can be modified to measure unstable structures:

$$\begin{aligned} \min_{\tilde{\mathbf{f}}, \delta \mathbf{q}, \alpha} \quad & \|\mathbf{f}_n^+\|_2^2 + \gamma \|\mathbf{f}_n^-\|_2^2 + \|\alpha\|_2^2 \\ \text{s.t.} \quad & \mathbf{A}_{eq} \mathbf{B} \tilde{\mathbf{f}} = -\mathbf{p} \\ & \mathbf{A}_{fr} \mathbf{B} \tilde{\mathbf{f}} \leq \mathbf{0} \\ & \mathbf{A}_{eq}^\top \delta \mathbf{q} = \delta \mathbf{d} \\ & f_{jkn}^+ (\delta d_{jkn}^i + \varepsilon) = 0 \\ & f_{jkn}^+ f_{jkn}^- = 0 \\ & \mathbf{f}_{jkt} = -\alpha_{jk}^i \delta \mathbf{d}_{jkt}^i \\ & |\delta \mathbf{d}_{jk}^i| \leq \eta \\ & \gamma, \varepsilon, \eta \geq 0 \\ & f_{jkn}^+, f_{jkn}^-, \alpha_{jk}^i, (\delta d_{jkn}^i + \varepsilon) \geq 0, \quad \forall i, j, k, \end{aligned} \quad (14)$$

The tensile forces are introduced in the objective function using a highly penalised weighting factor γ . As the RBE formulation, Eq. (14) allows for the description of non-feasible stress states still favouring solutions without tension.

3.3. Extending assembly data structure for complex assemblies

We utilise the assembly data structure described in [43] and its computational implementation available through [73] to handle all information for complex assemblies efficiently. For assemblies with non-convex blocks, Frick et al. [43] proposed the use of multiple convex blocks to discretise a non-convex compound block marking the additional new interfaces as *internal*. This convex decomposition step of complex assemblies, e.g. freeform shapes, is not straightforward, as it requires additional and specific algorithms.

In the present paper, we propose an alternative procedure that does not require any the additional convex decomposition step. Specifically, the interface C_{jk} is approximated through w_{jk} planar compact subinterfaces C_{jko} with $o \in \{1, \dots, w_{jk}\}$ (see [Fig. 5](#)).

All subinterfaces along with their corresponding local reference systems can be stored in the edge E_{jk} of the original directed graph $G(V, E)$. Therefore, constructing the equilibrium matrix \mathbf{A}_{eq} becomes straightforward, since all interfaces are indexed in a compatible way. Our current implementation still requires the interfaces to be discretised either manually or by using an auto-triangulation algorithm. Compared to the existing assembly data structure that requires convex decomposition, our extended version is more straightforward and easier to use.

4. Numerical benchmarks

We implemented CRA in a Python-based code using Pyomo as an open-source modelling language [74] and IPOPT as a solver of the nonlinear constrained optimisation problem [75]. Additionally, we utilise COMPAS (An open-source computational framework for collaboration and research in Architecture, Engineering, Fabrication, and Construction) [76] as our base for the data structure such that our method can be easily integrated into any desired CAD software. The results are visualised with OpenGL. All examples and benchmarks are performed on a MacBook Pro with a 2.9 GHz 6-Core Intel Core i9 Processor and 16 GB memory.

In this section, looking at geometric models with increasing complexity, we benchmark the CRA method against widely used engineering software such as 3DEC (DEM) [30] and nonlinear FE analysis using Sofistik [77]. In particular, the benchmarks will consider the limit state scenarios, such as finding the maximum tilting angle for which a structure is still stable. We will show how the use of CRA allows a correct evaluation of the limit state and aligns with the results obtained with commercial software.

The first benchmarks regard the three simple examples shown in Yao et al. [44] and Shin et al. [7]. [Table 1](#) reports the results from these previous works along with the ones obtained using CRA, 3DEC and an in-house implementation of RBE. All numerical methods, except for Variational Static Analysis (VSA) proposed by Yao et al. [44], return the same limit tilting angle obtained from analytic solutions. For the 3-legged π example, the RBE results proposed by Shin et al. [7] are a bit lower (0.4°) than the one obtained from our RBE implementation, which might relate to small differences due to remodelling. While VSA is still conservative compared to other numerical methods, Yao et al. [44] justified its conservative results as they are closer to small-scale model results, and they attributed the RBE overestimation to the improper treatment of the sliding. Conversely, Shin et al. [7] stated the difference between physical and numerical results was related to the imperfections on small-scale 3D-printed models, which might be taken into account through an arch thickness reduction of 13% [78]. Small-scale physical models are always affected by imperfections that, according to their size, can drastically redirect the internal stress state and can consistently lower the stability values [33,79]. In [Remark 1](#), we will show that the failure of the semicircular arch of [Table 1](#) is not due to the improper treatment of the sliding in RBE, meaning that the RBE result is theoretically correct in that specific case, i.e., for the perfect geometry. In addition, RBE results about the maximum tilting angle of masonry arch are aligned with well-known ones available in the literature [80–84]. For evaluation of the theoretical limit state, CRA provides users with accurate numerical results that align well with engineering software 3DEC.

Remark 1. Here, we discuss the *arch thick* model reported in [Table 1](#). The semicircular arch ([Fig. 6a](#)) having a thickness-to-radius ratio $t/r = 0.150$ is discretised with 36 voussoirs, and the friction angle is assumed equal to 43° as Shin et al. [7]. The RBE tilting test shows a maximum tilting angle of 8.2° . The internal stress state is represented through resultant forces (in green) as

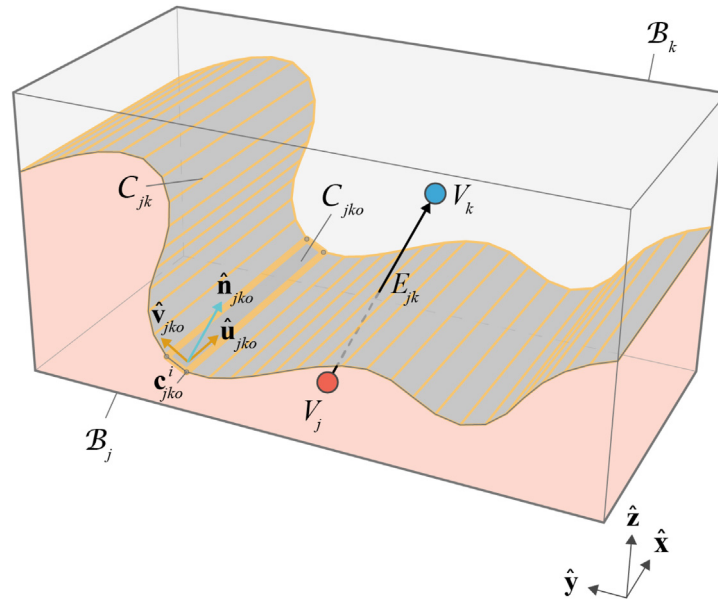


Fig. 5. The freeform interface C_{jk} can be approximated through many sub-interfaces C_{jko} .

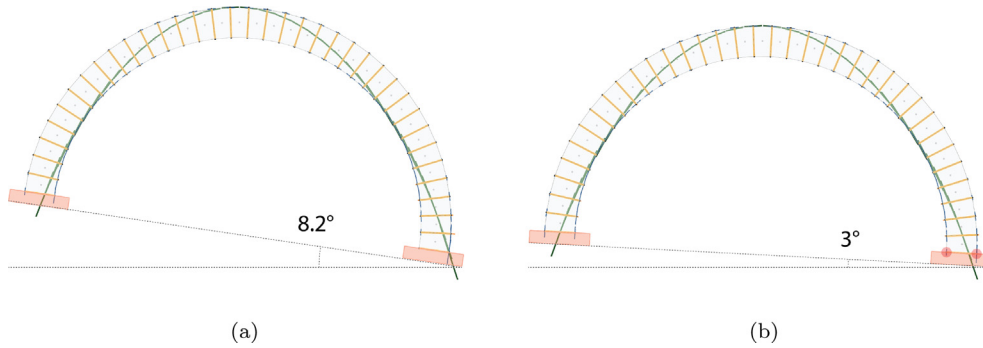


Fig. 6. Arch thick model. (a) With a friction angle equal to 43° , RBE returns a maximum tilting angle of 8.2° ; (b) while using a reduced friction angle of 21.8° , the maximum tilting angle is 3° . The red spheres denote the interface where a potential sliding motion is allowed. (For interpretation of the references to colour in this figure legend, the reader is referred to the web version of this article.)

from the combination of nodal forces over each interface. We label interfaces with red spheres when the nodal forces are in the limit state, i.e. lying on the boundary of the Mohr–Coulomb friction cone. As the reader can note, the resultants are everywhere within the friction cone as no interface is labelled in red. Thus, the limit friction capacity of the arch is not reached, and sliding does not occur. To show how the friction capacity can influence the result, we consider a reduced friction angle equal to 21.8° (Fig. 6b). In this case, the RBE analysis shows that the maximum tilting angle is 3.0° . As the reader can notice, in this case, the interface among the right support and the arch is labelled in red, meaning that the maximum friction capacity is reached, sliding can occur. The lower friction capacity restricts the solution space resulting in a lower maximum tilting angle. These analyses were carried out also with CRA and 3DEC obtaining the same results. Note that for these specific cases, RBE is able to correctly capture the failure mode. The difference with physical models is only due to imperfections and tolerances always affecting by small-scale models.

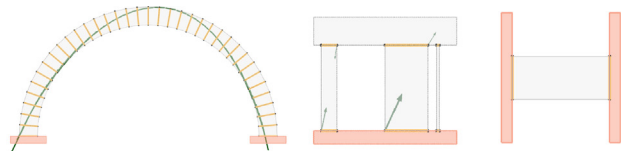
To show how our methodology can correctly capture non-feasible solutions and suggest non-stable regions, we perform the analysis of the shelf example provided in Yao et al. [44] (Fig. 7). Similarly to 3DEC, VSA correctly captures the sliding behaviour of two unstable elements. RBE, however, incorrectly

predicts the shelf as a stable structure. Differently from RBE, CRA without the penalty formulation (Eq. (11)) correctly classifies the model as non-stable, being the optimisation problem is infeasible. Applying the CRA penalty formulation (Eq. (14)), the model becomes feasible. Additionally, its result indicates the instability regions providing extra tensile forces required to make the structure stable. Fig. 7d shows that by providing a given amount of tensile capacity, represented by the red vector, the existing shelf design is in equilibrium. Therefore, CRA provides: (i) a correct assessment of unstable assembly, unlike RBE; (ii) in addition to VSA, quantitative information on what could be done to stabilise the design thanks to its penalty formulation.

Classic rigid-block models have been developed for planar interfaces and have not been applied to non-planar interfaces, particularly for sharp wedge connections. To the best of the authors' knowledge, these scenarios were not previously addressed in any study. However, real structures are often designed with complex and non-planar interfaces. With the third benchmark case, we want to address this problem. Fig. 8 shows four types of 3-block wedge models, similar to the one presented in Fig. 4: type-a and type-b have sharper wedge angles compared to type-c and type-d. Respectively, type-a and type-b have a lower the centre of mass compared to type-b and type-c. We perform tilting tests among three different axes to get maximum tilting angles in Table 2. All models are rotated counterclockwise and results are

Table 1

Benchmark table provided in Yao et al. [44] and Shin et al. [7], here extended to also include 3DEC, CRA, and in-house version of RBE as solvers. We use the same friction angle 43° as in all previous works. In these three examples, CRA aligns well with both analytic and engineering software solutions.



| | Arch thick ($t/r = 0.150$) | 3-legged π | Model H |
|--|---------------------------------|----------------|----------------|
| # Free blocks | 36 | 4 | 1 |
| # Fixed blocks | 2 | 1 | 2 |
| Stability at tilt angle θ° | Analytic | Stable | Unstable |
| | Experiment (Shin et al.) | Stable | - |
| | RBE (Shin et al.) | Stable | Stable |
| | Inverse FEM (Shin et al.) | Stable | - |
| | VSA (Yao et al.) | Stable | Unstable |
| | 3DEC | Stable | Unstable |
| | Our RBE implementation | Stable | Stable |
| | CRA | Stable | Unstable |
| Critical tilt angle θ° | Analytic | 8.2 | - |
| | Experiment (Shin et al.) | 4.7 ± 0.2 | 14.3 ± 0.2 |
| | RBE (Shin et al.) | 8.2 | 19.1 |
| | Inverse FEM (Shin et al.) | 8.2 | 19.1 |
| | VSA (Yao et al.) | 5.3 | 16.4 |
| | 3DEC | 8.2 | 19.5 |
| | Our RBE implementation | 8.2 | 19.5 |
| | CRA | 8.2 | 19.5 |

provided considering two different friction coefficients ($\mu = 0.2$ and $\mu = 0.84$). We want to point out that wedges with sharp angles (e.g. *type-a* and *type-b*) cannot be analysed with classic rigid-block models such as RBE, as they always return a feasible solution even in an upside-down configuration, e.g. model A.

In the comparison table, CRA aligns well with 3DEC results except for *type-c rotate-xy30*. We observe the different limit tilting angle is coming from the fundamental difference at the base of these two solvers. 3DEC is a dynamic solver, and it can capture the equilibrium on newly deformed configurations. Specifically, in the 3DEC analysis, between 40° and 48° , the free block slides slightly and settles reaching equilibrium in a new, deformed configuration. Performing a CRA analysis of the 3DEC deformed configuration, we get the same results, confirming that

it is stable. In this sense, CRA is slightly conservative because it only considers the static equilibrium on the initial configuration. RBE, in contrast, seems to have bad predictions for *sharp wedge* angles and standard friction coefficients, as also pointed out in Section 2.2 with the A model.

The last two examples look at simple assemblies with concave and curved interfaces in order to benchmark CRA when the extended version of the data structure is used. Fig. 9a and b show two concave shape joint geometries with the same interface but different cantilever lengths. We compare CRA results against 3DEC in a tilting test considering two friction values, i.e. friction coefficients 0.10 and 0.84 correspond to friction angles equal to 5.71° and 40.03° , respectively. As from Table 3, a very good agreement can be noted. In particular, the positions of the centre

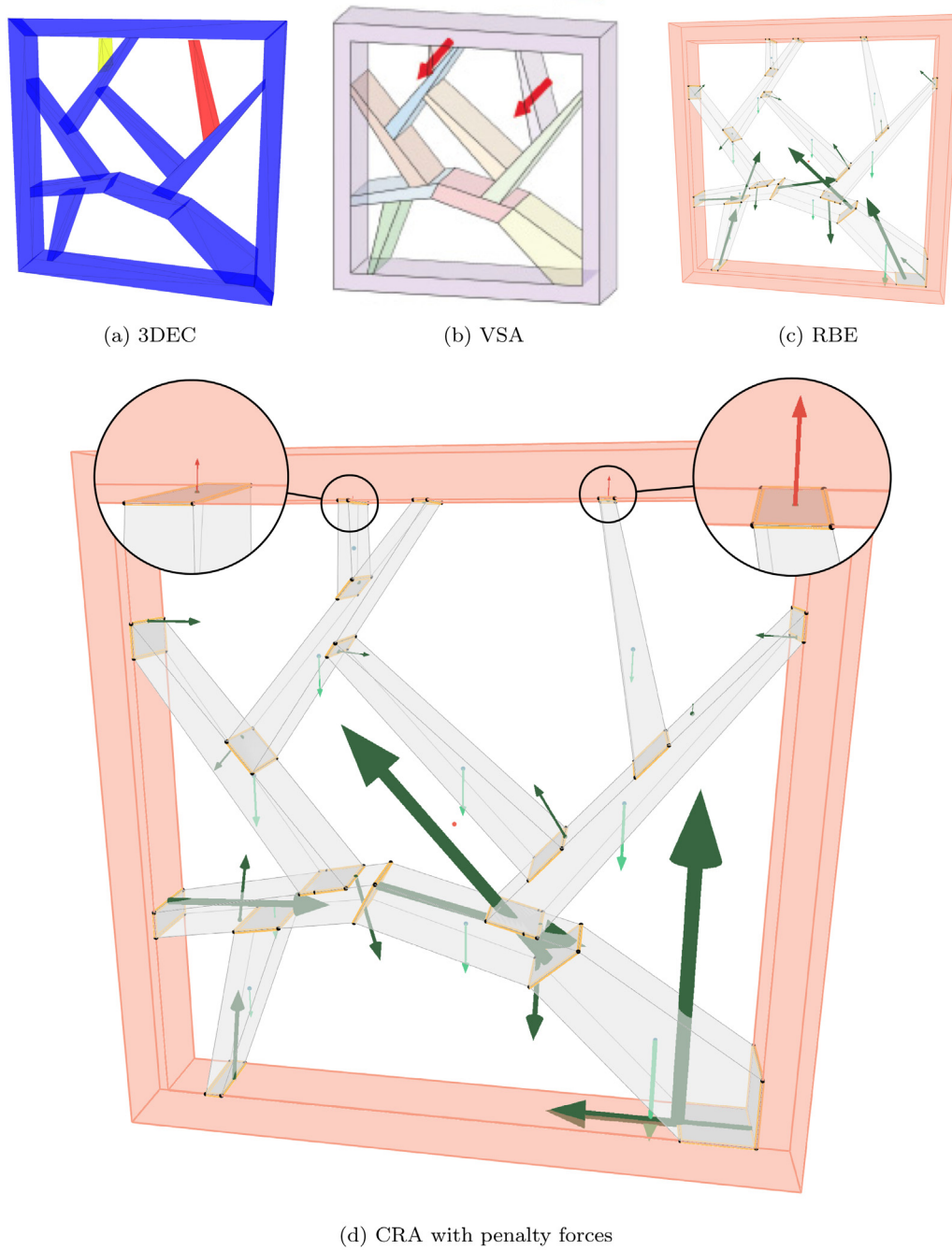


Fig. 7. Shelf model. (a) 3DEC analysis shows 2 unstable pieces with their sliding directions. (b) VSA shows similar results as 3DEC (image taken from Yao et al. [44]). (c) RBE incorrectly identifies the structure as stable. (d) the designer can use CRA not only to correctly identify unstable parts, but also to define the extra forces needed to make the assembly stable. (For interpretation of the references to colour in this figure legend, the reader is referred to the web version of this article.)

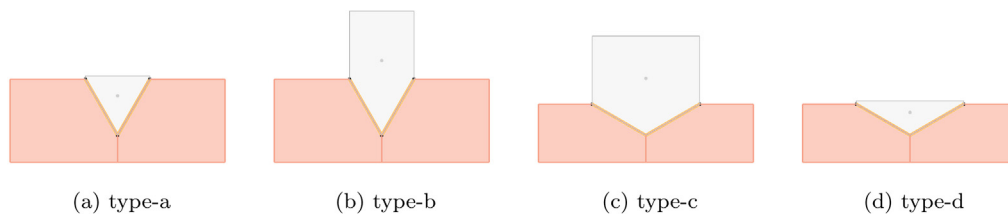


Fig. 8. 3-blocks wedge models. All models are initially placed vertically on the XY-plane with gravity pointing in the negative Z-axis and are viewed with a camera point towards the XZ-plane.

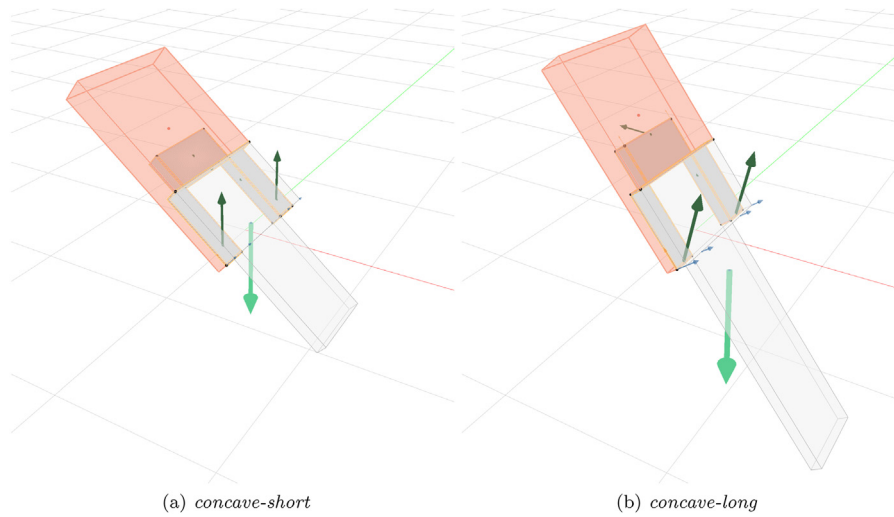


Fig. 9. The maximum tilt of two concave shape joint geometries with different lengths of cantilever. (a) and (b) are CRA results corresponding to the friction coefficient $\mu = 0.84$ in (c).

Table 2

Benchmark table for 3-blocks wedge models in Fig. 8. *rotate-x*, *rotate-y*, and *rotate-xy30* represent the results of the tilting tests using $(1, 0, 0)$, $(0, 1, 0)$, and $(\sqrt{3}, 1, 0)$ as rotation axes.

| Type | Rotation axis Angle (deg) | $\mu = 0.20$ | | | $\mu = 0.84$ | | |
|--------|------------------------------|--------------|------|------|--------------|-------|-------|
| | | 3DEC | CRA | RBE | 3DEC | CRA | RBE |
| type-a | rotate-x | 21.8 | 21.8 | 25.0 | 59.2 | 59.2 | 180.0 |
| | rotate-y | 71.3 | 71.3 | 71.3 | 100.0 | 100.0 | 180.0 |
| | rotate-xy30 | 24.8 | 24.7 | 28.0 | 62.7 | 62.9 | 180.0 |
| type-b | rotate-x | 21.8 | 21.8 | 25.0 | 58.7 | 58.5 | 180.0 |
| | rotate-y | 67.4 | 67.4 | 67.4 | 109.1 | 109.1 | 180.0 |
| | rotate-xy30 | 24.8 | 24.7 | 28.0 | 63.1 | 62.0 | 180.0 |
| type-c | rotate-x | 13.0 | 13.0 | 13.0 | 44.1 | 44.1 | 47.0 |
| | rotate-y | 41.3 | 41.3 | 41.3 | 64.5 | 64.4 | 65.7 |
| | rotate-xy30 | 14.9 | 14.9 | 15.0 | 48.1 | 40.2 | 51.0 |
| type-d | rotate-x | 13.0 | 13.0 | 13.0 | 44.1 | 44.1 | 50.0 |
| | rotate-y | 41.3 | 41.3 | 41.3 | 70.0 | 70.0 | 70.0 |
| | rotate-xy30 | 14.9 | 14.9 | 15.0 | 49.0 | 48.5 | 54.0 |

Table 3

Benchmark table for concave joints in Fig. 9.

| Type | Rotation axis Angle (deg) | $\mu = 0.84$ | | $\mu = 0.10$ | |
|---------------|------------------------------|--------------|-----|--------------|-----|
| | | 3DEC | CRA | 3DEC | CRA |
| concave-short | rotate-x | 40 | 40 | 5 | 5 |
| concave-long | rotate-xy | 56 | 54 | 10 | 9 |

of mass of these two models affect the results. Indeed, while in the *concave-short* model, the failure is due to the friction capacity on the two lateral contact sides, the *concave-long* can activate an additional contact on the back that makes it more stable. Moreover, as soon as the model is tilted to the limit angle, the low friction angle configuration starts to slide as expected.

Lastly, we benchmark CRA on three types of freeform assemblies with curved interfaces against 3DEC and Sofistik. The models and the corresponding results are reported in Fig. 10a, b, and Table 4. CRA directly discretises the original curved interface as described in Fig. 5. Conversely, 3DEC cannot take the curved interfaces into account directly; to analyse assembly with curved interfaces, we proceeded with a preprocessing modelling phase cutting each block into convex sub-blocks, which were joined together later. As this is not common, we also decided to benchmark CRA against Sofistik FE software. Sofistik can similarly handle curved interfaces, but it needs additional meshing

steps for generating triangular surface elements and tetrahedral volume elements. Moreover, Sofistik considers only one normal vector for each vertex averaging the normal vectors of the neighbouring faces.

Table 4 illustrates the tilting tests performed considering three qualitatively different models and assuming various distinct tilting directions.

In Fig. 10a, the *curve-3-blocks* model consists of three vertically stacked blocks with interfaces curved in the X-axis. In this case, we perform five tilting tests around different axes, and all CRA results align well with both 3DEC and Sofistik. In Fig. 10b and c, we model curved interfaces in both X-axis and Y-axis. Both *cube-curve-short* and *cube-curve-tall* have the same interface and discretisation. They are different in terms of their centre of mass positions. Due to the symmetry of the shape, we perform only three different tilting directions for both *cube-curve* models. For the *cube-curve-short* model, CRA seems to align well with 3DEC results. On the other hand, Sofistik seems slightly more conservative, especially for the *rotation-xy* axis. For the *cube-curve-tall* model, CRA gives a more conservative angle in the *rotation-xy* axis.

In general, CRA nicely captures the limiting state of different geometries and aligns well with engineering software solutions. The correct prediction of stability greatly enlarges the design space of discrete-element assemblies. In the next section, we will show some examples using CRA in the forward design process.

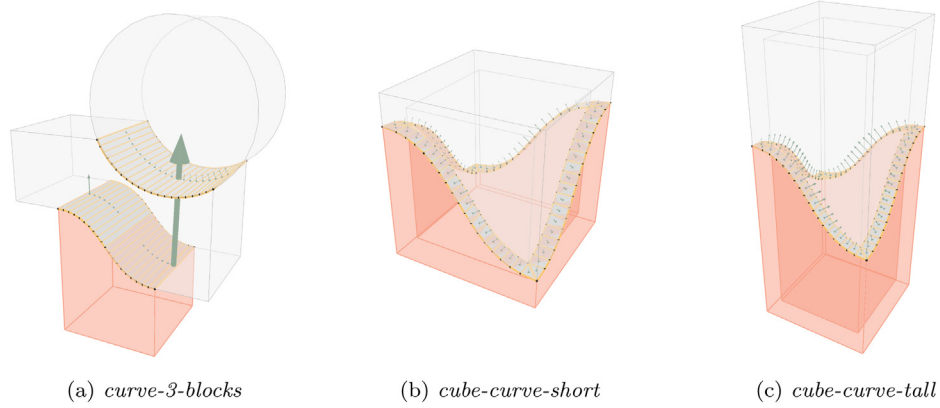


Fig. 10. The maximum tilting angle of three types of non-standard assembly shapes with curved interfaces.

Table 4

Benchmark table for non-standard assembly with curved interface in Fig. 10. All tilting angles are rotated anticlockwise according to a specific rotational axis, e.g. the *rotate-xy* represents the rotational vector (1, 1, 0) and *rotate-xny* represents the rotational vector (1, -1, 0).

| Type | Rotation axis | $\mu = 0.84$ | | | |
|------------------|---------------|--------------|----------|-----|-----|
| | Angle (deg) | 3DEC | Sofistik | CRA | RBE |
| curve-3-blocks | rotate-y | 8 | 8 | 8 | 8 |
| | rotate-ny | 53 | 53 | 53 | 53 |
| | rotate-x | 24 | 24 | 24 | 26 |
| | rotate-xy | 11 | 12 | 12 | 12 |
| | rotate-xny | 46 | 47 | 47 | 48 |
| cube-curve-short | rotate-x | 72 | 70 | 70 | 180 |
| | rotate-xy | 68 | 64 | 69 | 180 |
| | rotate-xny | 80 | 79 | 79 | 180 |
| cube-curve-tall | rotate-x | 41 | 38 | 40 | 180 |
| | rotate-xy | 39 | 38 | 39 | 180 |
| | rotate-xny | 59 | 58 | 51 | 180 |

5. Interactive stability-aware design process using CRA

As we stated in previous sections, CRA can assess stability correctly, and its penalty formulation can provide users with additional information. Section 5.1 shows how CRA can be integrated into an interactive stability-aware design workflow, while Section 5.2 shows its potential in guiding the designer towards a self-supporting shape.

5.1. Workflow

We propose a stability-aware design process and summarise it as an algorithm workflow in Fig. 11. The algorithm input is the user-provided assembly that includes geometry, mechanical parameters, boundary conditions, etc. Note that the definition/choice of the boundary condition allows selecting which blocks are considered as supports. In this sense, its use enables the possibility to assess local stability. After set up, the central analysis consists of two CRA formulations, with and without the penalty formulation, i.e. using optimisations (Eq. (11)) and (Eq. (14)) respectively. The algorithm first assesses the stability of the assembly using the optimisation problem (Eq. (11)). If the assembly is unstable (i.e. infeasible), the algorithm further analyses it with the CRA penalty form (Eq. (14)) to identify unstable regions. Once the unstable parts have been defined, the user can change the geometry accordingly to remove tensile forces until a satisfactory degree. In the next section, we will show how to use stability-aware design workflow to redirect design choices.

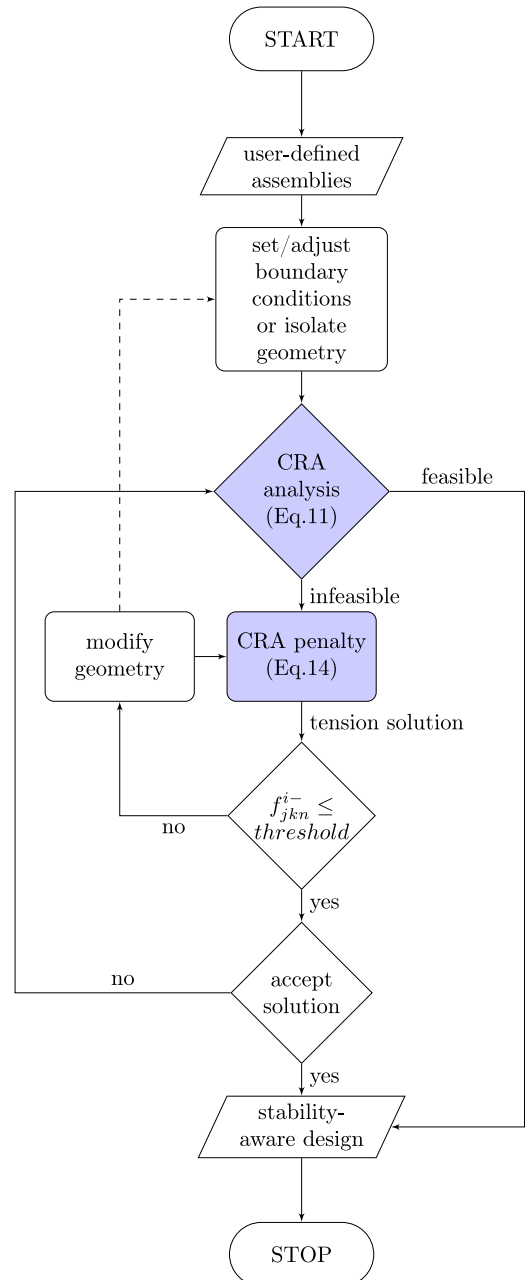


Fig. 11. CRA integration with stability-aware design workflow.

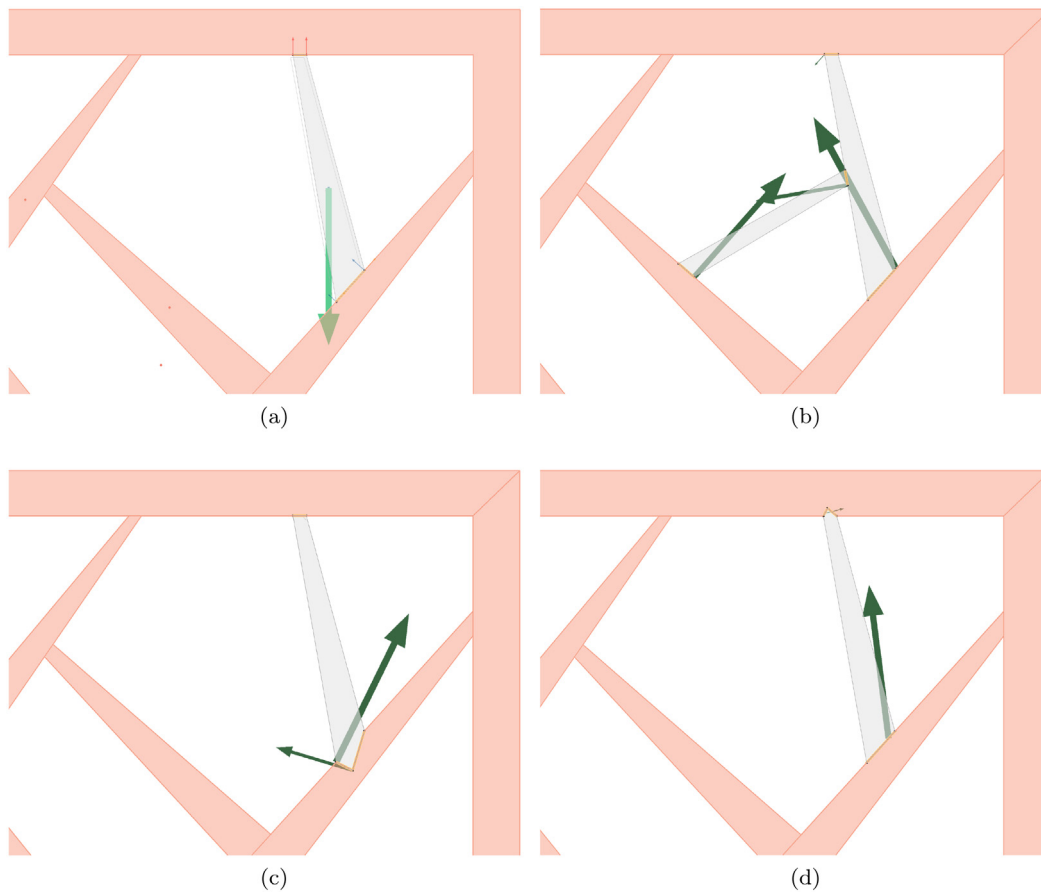


Fig. 12. The local instability can be understood better by isolating the unstable parts from the shelf model (Fig. 7). Tension forces on the top indicate the specific interface is not loaded, and the light grey rectangle shows the virtual displacement as potential sliding movement (a). The unstable element can be resolved by adding a supporting element (b), changing bottom interface geometry (c), or changing upper interface geometry (d).

5.2. Interactive process towards stability

In this section, looking at the shelf model, we demonstrate the effectiveness of the proposed workflow. Optimisation problems (11) is infeasible, meaning that the shelf is not stable. CRA with penalty formulation (Eq. (14)) shows two unstable elements (Fig. 7). After that, we apply CRA on each local element individually. E.g. looking at the top-right element, we set all its neighbouring parts as support. The tensile forces above the upper interface indicate that the region is not activated (Fig. 12a). In addition, the virtual displacement (light grey rectangle) shows the potential sliding direction. To prevent the element from sliding down and provide the uplifting force, we provide three possible modifications: adding an element as support (Fig. 12b) or changing the bottom (Fig. 12c) or the upper (Fig. 12d) interface geometry to enforce the resultant inside the friction cone. For each modification, CRA provides real-time feedback about the stability of the new configuration. The users can learn from the force feedback and modify their initial design by choice toward better local stability-aware design. After the instability of a specific local element is resolved, the user can resolve different unstable regions locally one by one until the entire structure reaches global equilibrium.

6. Results

In this section, we demonstrate that the accuracy of CRA enables a wide range of design possibilities. The analysis in Section 6.1 aims at illustrating that, even though it is based on a

nonlinear programming optimisation, CRA can be used to assess real structures composed of many elements.

The second and the third examples in Section 6.2 show two simple but meaningful design cases where CRA is used to assess and design self-supporting structures that can be assembled scaffold-free during assembly. Our designs are validated through scaled physical models that are 3D-printed with a Stratasys Objet500 Connex3 3D Printer.

6.1. Analysing complex structures

Fig. 13 shows the CRA analysis of the Armadillo Vault presented in Fig. 1a. The model consists of 399 blocks and 1014 interfaces. The built Armadillo Vault structure has a 16 metres span with a minimum block thickness of 5 cm [85,86]. In our numerical model, we approximate non-planar ruled surfaces to locally planar interfaces and identify the first layer of blocks as supports. Importantly, CRA correctly identifies the Armadillo Vault as a stable structure, even with such thin structural thickness. In addition, the internal resultant forces obtained from CRA nicely capture the arching and ringing actions as illustrated in Fig. 13.

6.2. Numerical analysis and physical models

The following example looks at the *snake* design, whose process is summarised in Fig. 14. The snake is composed of three pieces plus the supporting base. The ability to accurately model sharp interfaces with friction enables the user to reach

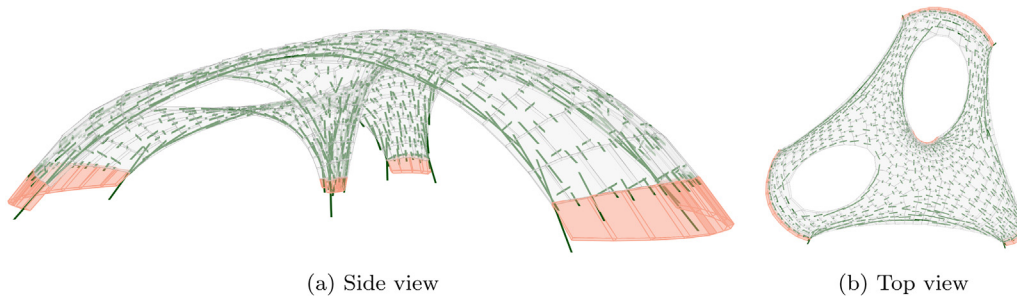


Fig. 13. CRA correctly identifies the Armadillo Vault (Fig. 1a) as a stable structure identifying arching and ringing actions correctly.

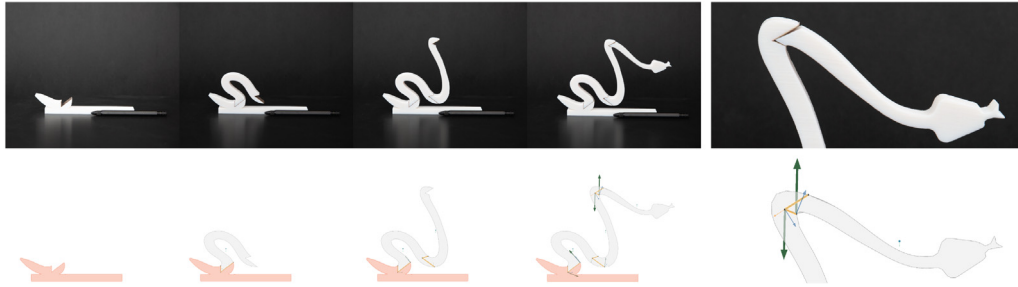


Fig. 14. Snake model: step-by-step construction sequence of both CRA analysis (bottom) and corresponding physical model (top). Friction value $\mu = 0.66$ is applied in the CRA analysis. Two images on the right highlight the detailed interface and forces of the assembled model.



Fig. 15. Sequential scaffolding-free construction of the bridge. CRA analyses on top and corresponding construction phases on the small-scale physical models on the bottom.

cantilevered solutions that are not possible with only planar interfaces. Note the parallels between the physical model and CRA result in Fig. 14. Because of small tolerances, the head of the snake moves slightly. However, the small movement emphasises that equilibrium is reached through the transmission of reaction forces on two contact points, which match the reaction forces found with the CRA analysis.

The last analysis regards a bridge design, whose assembly process together with the CRA results are summarised in Figs. 15 and 16. The bridge has been specifically designed to avoid interlocked joints but still have an assembly sequence such that each piece can stably stand without any additional scaffolding. To limit the effect of tolerances on the physical model, a connection (red circles in Fig. 16) is designed to have the first two pieces self-registered in the desired position. The friction coefficient adopted in the analysis is 0.66. A parametric CRA analysis showed that for friction values lower than 0.35, the bridge cannot be constructed scaffolding-free. As the friction coefficient of the printing material is around 0.3, we applied sandpapers to the interfaces to guarantee that the actual friction value is above 0.66. The sandpaper with double-sided tape has a thickness of 0.58 mm, which was carefully considered in the 3D printed geometry. The bridge stands under its self-weight, and as Fig. 16 shows, it can support additional loads. The bridge's net mass (i.e. without supports) is 319 g, while the mass of the external distributed loads is 1208 g. Fig. 16 shows the CRA results obtained considering these external, additional loads (i.e. to this aim, the additional blocks have a higher material density). Lastly, looking at the physical

model in Fig. 16b, the keystone is touching and transmitting forces only through the two upper interfaces. This phenomenon is well captured by the CRA analysis in Fig. 16a, where the solution returns only two resultants affecting those interfaces while the lower ones are not reacting, as highlighted with green circles.

7. Conclusion

The equilibrium approach is a common strategy for analysing the stability of rigid block assemblies. Nonetheless, existing methods are either too conservative or cannot provide realistic or accurate results even on some simple scenarios. This paper introduces a new method, named CRA, to assess the stability of complex assemblies. The CRA method provides accurate results that can push structural stability to the limit during assembly, consequently saving material and allowing for thinner complex structures.

Different from previous methods, CRA provides an accurate evaluation of internal stress states and limit scenarios thanks to a nonlinear programming formulation that couples equilibrium and kinematics. Beyond classical constraints representing the equilibrium and the friction capacity of the assembly, two additional and crucial constraints are considered. The first is a complementarity condition that relates detachment and normal forces: normal forces are not allowed when blocks are no longer in contact. The second constraint aligns friction forces with *virtual* sliding movements. Its use is particularly relevant to capture the stability of non-planar and sharp wedge connections.



Fig. 16. (a) Bridge in its final configuration and subjected to additional loads. (b) The span of the 3D printed model is 40 cm, the net mass of the bridge is 319 g, while the mass of the external loads is 1208 g. The red circles denote two *sharp wedges* designed to guarantee that the two external elements are in the right position. (For interpretation of the references to colour in this figure legend, the reader is referred to the web version of this article.)

Furthermore, this new nonlinear optimisation problem is rewritten in a penalty formulation, allowing us to evaluate non-equilibrated assemblies and thus explore a larger configuration space. It allows for the detection of non-stable regions, providing additional information to stabilise the assembly. Moreover, the existing graph-based assembly data structure has been extended to enable flexible analysis of complex shapes with curved interfaces. Importantly, CRA can be integrated into a proposed stability-aware design workflow to assist users towards more structurally-sound designs. The following essential aspects allowed by the proposed methodology should be highlighted:

- CRA enables correct stability assessments of connections with sharp wedge interfaces, which are not possible with existing equilibrium methods;
- In order to consider fabrication defects or assembly tolerances, we can use a lower friction value or reduced interface to obtain conservative results;
- The penalty formulation allows the user to redirect design choices. In our physical models, we also used the penalty formulation to obtain meaningful information about the discretisation process. CRA with penalty formulation not only suggests if the structure is stable but also improves our understanding of the structural response;
- The potential of our formulation is demonstrated on the cantilever bridge design, where the interfaces were iteratively designed using the proposed stability-aware design workflow to achieve stable solutions, both for the final structure and during assembly;
- An accurate description of the assembly internal stress state when coupled with corresponding small virtual displacements represents a robust overall strategy to understand the structural behaviour during the design process; and,
- Even though it is based on a nonlinear programming formulation, the computation time of CRA required for local stability analysis is satisfactory. Taking the Armadillo Vault – a real structure – as an example, we demonstrated that CRA is able to solve problems of practically relevant sizes and complexity.

Table 5 reports the computational burden listed for all the performed analyses.

To conclude, the potential of the proposed methodology has been demonstrated by designing some physical scale models in surprising equilibrium configurations, where the physical contacts among real blocks match the CRA interface forces.

The present formulation is based on nonlinear constrained optimisation. Thus, it does not guarantee global convergence and

Table 5

Performance of all examples, all solving times of models are analysed at the rest position without applying any tilting.

| Fig | Model | #Blocks | #(Sub)Interfaces | Solving time (sec) |
|-----|------------------|---------|------------------|--------------------|
| 6 | Arch thick | 38 | 37 | 1.02 |
| 7 | Shelf | 11 | 19 | 0.50 |
| 8a | type-a | 3 | 2 | 0.05 |
| 8b | type-b | 3 | 2 | 0.05 |
| 8c | type-c | 3 | 2 | 0.05 |
| 8d | type-d | 3 | 2 | 0.05 |
| 9a | concave-short | 2 | 7 | 0.23 |
| 9b | concave-long | 2 | 7 | 0.15 |
| 10a | curve-3-blocks | 3 | 40 | 2.38 |
| 10b | cube-curve-short | 2 | 72 | 1.15 |
| 10c | cube-curve-tall | 2 | 72 | 1.04 |
| 13 | Armadillo Vault | 399 | 1014 | 2424.44 |
| 14 | Snake | 4 | 7 | 0.35 |
| 15 | Completed bridge | 11 | 33 | 1.27 |
| 16 | Bridge with load | 16 | 38 | 1.26 |

different starting points may result in different local optima. Parallel programming and other nonlinear solving algorithms will be investigated to speed up the solving time.

Two aspects can be further enhanced: i) use of a sequential optimisation procedure superimposing small displacements at each step to capture equilibrated solutions on a deformed but still safe configuration; ii) the introduction of specific algorithms to generate complex curved interface patterns to explore more stable solutions.

Finally, we want to point out that CRA with its penalty formulation represents an ideal basis for automatic shape optimisation of initially infeasible configurations.

Declaration of competing interest

The authors declare that they have no known competing financial interests or personal relationships that could have appeared to influence the work reported in this paper.

Acknowledgements

We would like to express our thanks to our colleagues Keerthana Udaykumar for assisting with 3D printed model making, Francesco Ranaudo and Sam Bouten for helpful discussion regarding the structural analysis, Alessandro Dell'Endice's help for 3DEC, and Dr Noelle Paulson for proofreading. Specifically, we like to thank Gene's good friends Lenny Fan and Dr Lucas Peng for many insightful theoretical discussions from both mathematics and physics perspectives. This research was supported

by the NCCR Digital Fabrication, funded by the Swiss National Science Foundation (NCCR Digital Fabrication Agreement # 51NF40-141853) and by the SNSF – Swiss National Science Foundation (Project number 178953: ‘Practical Stability Assessment Strategies for Vaulted Unreinforced Masonry Structures’).

Appendix A. Equilibrium equations

Referring to Fig. 2, we detail the equilibrium equation using the same notation adopted in Section 2.1. For the assembly \mathcal{A} with l blocks and h interfaces to be in static equilibrium requires that every block has to be in equilibrium. In particular, six equilibrium equations can be written, three for the net force and three for the torques. Looking at the block \mathcal{B}_k , the equilibrium equations due to all nodal reaction forces \mathbf{f}_{jk} acting on the m_{jk} -sided polygonal interface \mathcal{C}_{jk} can be compactly expressed as:

$$\mathbf{A}_{k,jk} \mathbf{f}_{jk} = \begin{bmatrix} \mathbf{a}_{jk,x} & \mathbf{a}_{jk,y} & \mathbf{a}_{jk,z} \\ \mathbf{b}_{jk,x}^1 & \mathbf{b}_{jk,x}^2 & \mathbf{b}_{jk,x}^m \\ \mathbf{b}_{jk,y}^1 & \mathbf{b}_{jk,y}^2 & \mathbf{b}_{jk,y}^m \\ \mathbf{b}_{jk,z}^1 & \mathbf{b}_{jk,z}^2 & \mathbf{b}_{jk,z}^m \end{bmatrix} \begin{bmatrix} \mathbf{f}_{jk}^1 \\ \mathbf{f}_{jk}^2 \\ \vdots \\ \mathbf{f}_{jk}^m \end{bmatrix},$$

where $\mathbf{a}_{jk,i} = [\hat{n}_{jk,i} \ \hat{u}_{jk,i} \ \hat{v}_{jk,i}]$, $\mathbf{b}_{jk,i} = [(\mathbf{r}_{kj}^i \times \hat{n}_{jk,i})_i \ (\mathbf{r}_{kj}^i \times \hat{u}_{jk,i})_i \ (\mathbf{r}_{kj}^i \times \hat{v}_{jk,i})_i]$, $i \in \{x, y, z\}$, and $\mathbf{f}_{jk}^i = [f_{jkn}^i \ f_{jku}^i \ f_{jkv}^i]^T$. Particularly, $\hat{n}_{jk,x}$, $\hat{u}_{jk,x}$, and $\hat{v}_{jk,x}$ are the x coordinate of the \mathcal{C}_{jk} 's basis in global reference systems. The \mathbf{r}_{kj}^i is the torque arm vector pointing from mass centre of \mathcal{B}_k to \mathbf{c}_{jk}^i . The first three rows of $\mathbf{A}_{k,jk}$ collect the translational coefficients, while the last three rows collect the torque coefficients. These six equilibrium equations have to be written for all interfaces \mathcal{C}_{jk} among \mathcal{B}_k and each of its neighbouring blocks \mathcal{B}_j . Once collected all equilibrium equations for all blocks, the global equilibrium of the entire assembly \mathcal{A} reads:

$$\mathbf{A}_{eq} \mathbf{f} = -\mathbf{p}$$

$$\begin{bmatrix} \mathbf{A}_{1,1} & \cdots & \mathbf{A}_{1,h} \\ \vdots & \ddots & \vdots \\ \mathbf{A}_{l,1} & \cdots & \mathbf{A}_{l,h} \end{bmatrix} \begin{bmatrix} \mathbf{f}_1 \\ \vdots \\ \mathbf{f}_h \end{bmatrix} = - \begin{bmatrix} \mathbf{p}_1 \\ \vdots \\ \mathbf{p}_l \end{bmatrix},$$

where the row k and the column j of sub matrix element $\mathbf{A}_{k,j}$ represent equilibrium equations of \mathcal{B}_k as coming from interface \mathcal{C}_j . Note that all interfaces \mathcal{C}_{jk} are collected in a given order through the map $g : \mathcal{C}_{jk} \in \mathcal{C} \mapsto \mathcal{C}_j \in \mathcal{C}$ and $j \in \{1, \dots, h\}$. Typically, \mathbf{A}_{eq} is sparse. Indeed, each column j only has at most two non-zeros sub-matrices $\mathbf{A}_{k,j}$ as each interface is shared by two adjacent neighbouring blocks. Besides, if the block \mathcal{B}_k is a support, the corresponding sub-matrix is zero. Specifically, the row k in the equation, $[\mathbf{A}_{k,1} \ \cdots \ \mathbf{A}_{k,h}] [\mathbf{f}_1 \ \cdots \ \mathbf{f}_h]^T = -\mathbf{p}_k$, represents the equilibrium condition for \mathcal{B}_k respective to all its neighbouring interfaces, where \mathbf{p}_k is the vector collecting the external loads acting on the \mathcal{B}_k . For Eq. (3), the different dimensional $\tilde{\mathbf{f}}$ is represented element-wise $\tilde{\mathbf{f}}_{jk} = [f_{jkn}^{i+} \ f_{jkn}^{i-} \ f_{jku}^i \ f_{jkv}^i]^T$ and \mathbf{B} is a matrix that maps $\tilde{\mathbf{f}}$ to \mathbf{f} . We define this relation as $\mathbf{B}_{jk}^i \tilde{\mathbf{f}}_{jk} = \mathbf{f}_{jk}^i$ with:

$$\mathbf{B}_{jk}^i = \begin{bmatrix} 1 & -1 & 0 & 0 \\ 0 & 0 & 1 & 0 \\ 0 & 0 & 0 & 1 \end{bmatrix} \quad \forall i, j, k.$$

Appendix B. Linearised friction constraint

We detail the eight-sided linearised friction constraint of Eq. (5). Theoretically, the Mohr–Coulomb criterion is represented

by a cone. Nonetheless, to speed up the process, it is common to approximate the original cone with a pyramid. Fig. B.17 shows an eight-sided cone approximation and its vertex coordinates concerning two tangential axes \mathbf{f}_{jkn}^i and \mathbf{f}_{jkv}^i .

Looking at an interface's vertex, Eq. (4) can be rewritten through the two following inequalities:

$$-\mu f_{jkn}^{i+} + f_{jkt}^i \leq 0$$

$$-\mu f_{jkn}^{i+} - f_{jkt}^i \leq 0, \quad \forall i, j, k.$$

If we replace f_{jkt}^i with f_{jku}^i and f_{jkv}^i , we can define the eight-sided approximation of the Mohr–Coulomb criterion as:

$$\mathbf{G}_{jk}^i \tilde{\mathbf{f}}_{jk} \leq \mathbf{0}, \quad \forall i, j, k,$$

where \mathbf{G} matrix is:

$$\begin{bmatrix} -\mu & 1 & 0 \\ -\mu & 0 & 1 \\ -\mu & -1 & 0 \\ -\mu & 0 & -1 \\ -\mu & 1/\sqrt{2} & 1/\sqrt{2} \\ -\mu & -1/\sqrt{2} & 1/\sqrt{2} \\ -\mu & -1/\sqrt{2} & -1/\sqrt{2} \\ -\mu & 1/\sqrt{2} & -1/\sqrt{2} \end{bmatrix},$$

\mathbf{B}_{jk}^i matrix is:

$$\mathbf{B}_{jk}^i = \begin{bmatrix} 1 & 0 & 0 & 0 \\ 0 & 0 & 1 & 0 \\ 0 & 0 & 0 & 1 \end{bmatrix} \quad \forall i, j, k,$$

and it can be stacked into a big diagonal matrix considering all vertices of all interfaces:

$$\mathbf{A}_{fr} \mathbf{B} \tilde{\mathbf{f}} = \begin{bmatrix} \mathbf{G} & & \\ & \ddots & \\ & & \mathbf{G} \end{bmatrix} \begin{bmatrix} \mathbf{B}_{jk}^i & & \\ & \ddots & \\ & & \mathbf{B}_{jk}^i \end{bmatrix} \begin{bmatrix} \tilde{\mathbf{f}}_1 \\ \vdots \\ \tilde{\mathbf{f}}_s \end{bmatrix} \leq \mathbf{0},$$

where $[\tilde{\mathbf{f}}_1 \ \cdots \ \tilde{\mathbf{f}}_s]^T$ are all the nodal forces.

Appendix C. Positiveness of the external work

Not all rigid motions can be physically possible, meaning that the space of kinematically admissible displacement has to be defined considering specific constraints. Beyond the local constraints expressing the non-overlapping of interfaces, a global requirement is that the work done by the external forces and the corresponding displacements has to be positive as expressed by Eq. (12). However, this requirement is implicitly taken into account by the constraints of the problem (11). Indeed, it results in:

$$\mathbf{p}^T \delta \mathbf{q} = -(\mathbf{A}_{eq} \mathbf{f})^T \delta \mathbf{q} = -\mathbf{f}^T \mathbf{A}_{eq}^T \delta \mathbf{q} = -\mathbf{f}^T \delta \mathbf{d},$$

with the last scalar product that can be decomposed into the sum of the work done by the normal and tangential contact forces and the dual contact displacements, as:

$$-\mathbf{f}_t^T \delta \mathbf{d}_t - \mathbf{f}_n^T \delta \mathbf{d}_n.$$

Note that the first term is always positive because of Eq. (9), while the normal coupling (Eq. (10)) the second term is close to zero. Thus it results in:

$$\mathbf{p}^T \delta \mathbf{q} = \sum_{i,j,k} \alpha_{jk}^i (\delta \mathbf{d}_{jkt}^i)^2,$$

showing that Eq. (12) holds as all α_{jk}^i are non-negative. ■

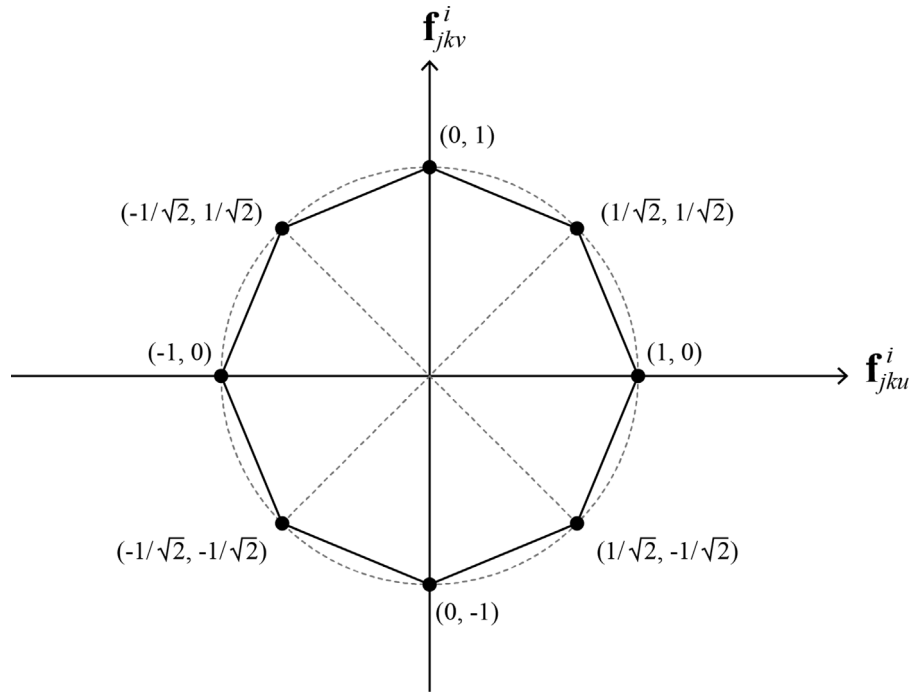


Fig. B.17. Eight-sided linearised friction cone.

Appendix D. List of symbols

| Symbol | Description |
|---|---|
| \mathcal{A} | Assembly set |
| \mathcal{B} | Block set |
| \mathcal{C} | Interface set |
| C_{jk} | Polygonal planar interface between block j and k |
| \mathbf{c}_{jk}^i | i th vertex of C_{jk} interface |
| $G(V, E)$ | Graph representing the assembly \mathcal{A} data structures |
| V | Vertices of the graph $G(V, E)$ |
| E | Directed edges of the graph $G(V, E)$ |
| \mathbf{w} | Self-weight of block |
| μ | Friction coefficient |
| \mathbf{r}_{kj}^i | The torque arm vector pointing from mass centre of \mathcal{B}_k to \mathbf{c}_{jk}^i |
| \mathbf{A}_{eq} | Equilibrium matrix |
| \mathbf{A}_{fr} | Matrix enforcing the linearised Mohr–Coulomb yield criterion |
| $(\hat{\mathbf{u}}_{jk}, \hat{\mathbf{v}}_{jk}, \hat{\mathbf{n}}_{jk})$ | Local reference system of interface C_{jk} |
| m_{jk} | Total number of vertices \mathbf{c}_{jk}^i of interface C_{jk} |
| \mathbf{f}_{jk} | Unknown nodal force vector acting on the vertex \mathbf{c}_{jk}^i of the interface C_{jk} |
| \mathbf{f}_{jku}^i | Interface's force \mathbf{f}_{jk}^i tangential component in $\hat{\mathbf{u}}_{jk}$ direction |
| \mathbf{f}_{jkv}^i | Interface's force \mathbf{f}_{jk}^i tangential component in $\hat{\mathbf{v}}_{jk}$ direction |
| \mathbf{f}_{jkn}^i | Interface's force \mathbf{f}_{jk}^i normal component in $\hat{\mathbf{n}}_{jk}$ direction |
| \mathbf{f}_{jkt}^i | Interface's tangential force on \mathbf{c}_{jk}^i |
| \mathbf{p} | Vector collecting the external forces as acting on the blocks' centroids |
| f_{jkn}^{i+} | Positive component of the normal force \mathbf{f}_{jkn}^i |
| f_{jkn}^{i-} | Negative component of the normal force \mathbf{f}_{jkn}^i |

| | |
|-----------------------------|--|
| \mathbf{f} | Vector collecting all interface force components wrt the $(\hat{\mathbf{n}}_{jk}, \hat{\mathbf{u}}_{jk}, \hat{\mathbf{v}}_{jk})$ local reference system |
| $\tilde{\mathbf{f}}$ | Vector collecting all interface force components wrt the $(+\hat{\mathbf{n}}_{jk}, -\hat{\mathbf{n}}_{jk}, \hat{\mathbf{u}}_{jk}, \hat{\mathbf{v}}_{jk})$ local reference system |
| \mathbf{B} | Matrix mapping $\tilde{\mathbf{f}}$ to \mathbf{f} |
| \mathbf{H} | Diagonal square matrix collecting the force components' weights |
| $\delta \mathbf{q}_k$ | Vector collecting the six Lagrangian parameters of \mathcal{B}_k |
| $\delta \mathbf{d}_{jku}^i$ | Tangential component in the $\hat{\mathbf{u}}_{jk}$ of the relative virtual displacement between block j and k on \mathbf{c}_{jk}^i |
| $\delta \mathbf{d}_{jkv}^i$ | Tangential component in the $\hat{\mathbf{v}}_{jk}$ of the relative virtual displacement between block j and k on \mathbf{c}_{jk}^i |
| $\delta \mathbf{d}_{jkn}^i$ | Tangential component in the $\hat{\mathbf{n}}_{jk}$ of the relative virtual displacement between block j and k on \mathbf{c}_{jk}^i |
| $\delta \mathbf{d}_{jkt}^i$ | Interface's nodal tangential virtual displacement on \mathbf{c}_{jk}^i |
| α_{jk}^i | Non-negative parameter to align friction force \mathbf{f}_{jkt}^i direction with relative sliding displacement $\delta \mathbf{d}_{jkt}^i$ |
| ε | Small numerical overlap parameter (i.e. 10^{-5} - 10^{-4} of the block dimension) |
| η | Limit value defining the max allowable displacement |
| γ | Weighting factor for penalising negative normal force |

References

- [1] Rippmann M, Van Mele T, Popescu M, Augustynowicz E, Méndez Echenaguia T, Calvo Barentin CJ, Frick U, Block P. The armadillo vault: Computational design and digital fabrication of a freeform stone shell. In: Advances in architectural geometry 2016. vdf Hochschulverlag AG; 2016, p. 344–63.

- [2] Safdie M, et al. Safdie architects habitat '67. 1967, URL <https://www.safdiearchitects.com/projects/habitat-67>.
- [3] Wagner HJ, Alvarez M, Groenewolt A, Menges A. Towards digital automation flexibility in large-scale timber construction: integrative robotic prefabrication and co-design of the BUGA Wood Pavilion. *Construct Robot* 2020;4(3):187–204.
- [4] Block P, Ciblac T, Ochsendorf J. Real-time limit analysis of vaulted masonry buildings. *Comput Struct* 2006;84(29–30):1841–52.
- [5] Dejong MJ. Seismic assessment strategies for masonry structures (Ph.D. thesis), Massachusetts Institute of Technology; 2009.
- [6] Whiting E. Design of structurally-sound masonry buildings using 3d static analysis (Ph.D. thesis), Massachusetts Institute of Technology; 2012.
- [7] Shin HV, Porst CF, Vouga E, Ochsendorf J, Durand F. Reconciling elastic and equilibrium methods for static analysis. *ACM Trans Graph (TOG)* 2016;35(2):1–16.
- [8] Papadopoulos KA. Seismic stability assessment of an ancient dry stone defensive wall. *Bull Earthq Eng* 2021;19(1):463–82.
- [9] Vouga E, Höbinger M, Wallner J, Pottmann H. Design of self-supporting surfaces. *ACM Trans Graph (TOG)* 2012;31(4):1–11.
- [10] Panozzo D, Block P, Sorkine-Hornung O. Designing unreinforced masonry models. *ACM Trans Graph (TOG)* 2013;32(4):1–12.
- [11] Deuss M, Panozzo D, Whiting E, Liu Y, Block P, Sorkine-Hornung O, Pauly M. Assembling self-supporting structures. *ACM Trans Graph* 2014;33(6): 214–1.
- [12] Block P, Ochsendorf J. Thrust network analysis: a new methodology for three-dimensional equilibrium. *J Int Assoc Shell Spat Struct* 2007;48(3):167–73.
- [13] Rippmann M, Lachauer L, Block P. Interactive vault design. *Int J Space Struct* 2012;27(4):219–30.
- [14] Baraff D. Coping with friction for non-penetrating rigid body simulation. *ACM SIGGRAPH Comput Graph* 1991;25(4):31–41.
- [15] Baraff D. Issues in computing contact forces for non-penetrating rigid bodies. *Algorithmica* 1993;10(2):292–352.
- [16] Baraff D. Fast contact force computation for nonpenetrating rigid bodies. In: *Proceedings of the 21st annual conference on computer graphics and interactive techniques*. 1994, p. 23–34.
- [17] Mattikalli R, Baraff D, Khosla P, Repetto B. Gravitational stability of frictionless assemblies. *IEEE Trans Robot Autom* 1995;11(3):374–88.
- [18] Mattikalli R, Baraff D, Khosla P. Finding all stable orientations of assemblies with friction. *IEEE Trans Robot Autom* 1996;12(2):290–301.
- [19] Guendelman E, Bridson R, Fedkiw R. Nonconvex rigid bodies with stacking. *ACM Trans Graph (TOG)* 2003;22(3):871–8.
- [20] Erleben K. Velocity-based shock propagation for multibody dynamics animation. *ACM Trans Graph (TOG)* 2007;26(2):12–es.
- [21] Stewart DE, Trinkle JC. An implicit time-stepping scheme for rigid body dynamics with inelastic collisions and coulomb friction. *Int J Numer Methods Eng* 1996;39(15):2673–91.
- [22] Mason MT, Wang Y. On the inconsistency of rigid-body frictional planar mechanics. In: *Proceedings. 1988 IEEE international conference on robotics and automation*. IEEE; 1988, p. 524–8.
- [23] Palmer RS. Computational complexity of motion and stability of polygons. Tech. rep., Cornell University; 1989.
- [24] Pang J-S, Trinkle J. Stability characterizations of rigid body contact problems with coulomb friction. *ZAMM Z Angew Math Mech* 2000;80(10):643–63.
- [25] Mosemann H, Rohrdanz F, Wahl FM. Stability analysis of assemblies considering friction. *IEEE Trans Robot Autom* 1997;13(6):805–13.
- [26] Kaufman DM, Sueda S, James DL, Pai DK. Staggered projections for frictional contact in multibody systems. In: *ACM SIGGRAPH Asia 2008 papers*. 2008, p. 1–11.
- [27] Goyal S, Ruina A, Papadopoulos J. Planar sliding with dry friction part 1. limit surface and moment function. *Wear* 1991;143(2):307–30.
- [28] Haas-Heger M, Ciocarlie M. Accurate energetic constraints for passive grasp stability analysis. *IEEE Trans Robot* 2020;36(4):1079–95.
- [29] Cundall PA. A computer model for simulating progressive, large-scale movement in blocky rock system. In: *Proceedings Of The International Symposium On Rock Mechanics*, 1971. 1971.
- [30] Itasca U. 3DEC—3 Dimensional Distinct Element Code. Minneapolis: Itasca Consulting Group Inc.; 2013.
- [31] Lemos J. Assessment of the ultimate load of a masonry arch using discrete elements. *Comput Methods Struct Mason* 1995;3:294–302.
- [32] Iannuzzo A, Dell'Endice A, Van Mele T, Block P. Numerical limit analysis-based modelling of masonry structures subjected to large displacements. *Comput Struct* 2021;242:106372.
- [33] Dell'Endice A, Iannuzzo A, Dejong MJ, Van Mele T, Block P. Modelling imperfections in unreinforced masonry structures: Discrete element simulations and scale model experiments of a pavilion vault. *Eng Struct* 2021;228:111499.
- [34] Bui T-T, Limam A, Sarhosis V, Hjiat M. Discrete element modelling of the in-plane and out-of-plane behaviour of dry-joint masonry wall constructions. *Eng Struct* 2017;136:277–94.
- [35] Sarhosis V, Bagi K, Lemos JV, Milani G. Computational modeling of masonry structures using the discrete element method. IGI Global; 2016.
- [36] Sarhosis V, Oliveira DV, Lemos JV, Lourenço PB. The effect of skew angle on the mechanical behaviour of masonry arches. *Mech Res Commun* 2014;61:53–9.
- [37] Fu C-W, Song P, Yan X, Yang LW, Jayaraman PK, Cohen-Or D. Computational interlocking furniture assembly. *ACM Trans Graph (TOG)* 2015;34(4):1–11.
- [38] Tai AS-C. Design for assembly: a computational approach to construct interlocking wooden frames (Ph.D. thesis), Massachusetts Institute of Technology; 2012.
- [39] Wang Z, Song P, Pauly M. DESIA: A general framework for designing interlocking assemblies. *ACM Trans Graph (TOG)* 2018;37(6):1–14.
- [40] Schwartzburg Y, Pauly M. Fabrication-aware design with intersecting planar pieces. In: *Computer graphics forum*. vol. 32, Wiley Online Library; 2013, p. 317–26.
- [41] Testuz RP, Schwartzburg Y, Pauly M. Automatic generation of constructable brick sculptures. Tech. rep., 2013.
- [42] Song P, Deng B, Wang Z, Dong Z, Li W, Fu C-W, Liu L. CofiFab: coarse-to-fine fabrication of large 3D objects. *ACM Trans Graph (TOG)* 2016;35(4):1–11.
- [43] Frick U, Van Mele T, Block P. Data management and modelling of complex interfaces in imperfect discrete-element assemblies. In: *Proceedings of IASS annual symposia*. vol. 2016, International Association for Shell and Spatial Structures (IASS); 2016, p. 1–9.
- [44] Yao J, Kaufman DM, Gingold Y, Agrawala M. Interactive design and stability analysis of decorative joinery for furniture. *ACM Trans Graph (TOG)* 2017;36(2):1–16.
- [45] Luo S-J, Yue Y, Huang C-K, Chung Y-H, Imai S, Nishita T, Chen B-Y. Legolization: Optimizing lego designs. *ACM Trans Graph (TOG)* 2015;34(6):1–12.
- [46] Kao GT, Körner A, Sonntag D, Nguyen L, Menges A, Knippers J. Assembly-aware design of masonry shell structures: a computational approach. In: *Proceedings of IASS annual symposia*. vol. 2017, (23):International Association for Shell and Spatial Structures (IASS); 2017, p. 1–10.
- [47] Bruun EP, Pastrana R, Paris V, Beghini A, Pizzigoni A, Parascho S, Adriaenssens S. Three cooperative robotic fabrication methods for the scaffold-free construction of a masonry arch. *Autom Construct* 2021;129:103803.
- [48] Whiting E, Ochsendorf J, Durand F. Procedural modeling of structurally-sound masonry buildings. In: *ACM SIGGRAPH Asia 2009 papers*. 2009, p. 1–9.
- [49] Whiting E, Shin H, Wang R, Ochsendorf J, Durand F. Structural optimization of 3D masonry buildings. *ACM Trans Graph (TOG)* 2012;31(6):1–11.
- [50] Livesley RK. Limit analysis of structures formed from rigid blocks. *Int J Numer Methods Eng* 1978;12(12):1853–71.
- [51] Livesley RK. A computational model for the limit analysis of three-dimensional masonry structures. *Meccanica* 1992;27(3):161–72.
- [52] Wang Z, Song P, Isvoranu F, Pauly M. Design and structural optimization of topological interlocking assemblies. *ACM Trans Graph (TOG)* 2019;38(6):1–13.
- [53] Wang Z, Song P, Pauly M. MOCCA: modeling and optimizing cone-joints for complex assemblies. *ACM Trans Graph (TOG)* 2021;40(4):1–14.
- [54] Kao GT-C, Iannuzzo A, Coros S, Van Mele T, Block P. Understanding rigid-block equilibrium method via mathematical programming. *Proc Inst Civ Eng Eng Comput Mech* 2021;1–39.
- [55] Shao T, Monszpart A, Zheng Y, Koo B, Xu W, Zhou K, Mitra NJ. Imagining the unseen: Stability-based cuboid arrangements for scene understanding. *ACM Trans Graph* 2014;33(6).
- [56] Hsu S-W, Keyser J. Automated constraint placement to maintain pile shape. *ACM Trans Graph (TOG)* 2012;31(6):1–6.
- [57] Beyeler L, Bazin J-C, Whiting E. A graph-based approach for discovery of stable deconstruction sequences. In: *Advances in architectural geometry 2014*. Springer; 2015, p. 145–57.
- [58] Frick U, Van Mele T, Block P. Decomposing three-dimensional shapes into self-supporting, discrete-element assemblies. In: *Modelling behaviour*. Springer; 2015, p. 187–201.
- [59] Mousavian E, Casapulla C. Structurally informed design of interlocking block assemblages using limit analysis. *J Comput Des Eng* 2020;7(4):448–68.
- [60] Bhooshan S, Van Mele T, Block P. Equilibrium-aware shape design for concrete printing. In: *Humanizing digital reality*. Springer; 2018, p. 493–508.
- [61] Wang Z, Song P, Pauly M. State of the art on computational design of assemblies with rigid parts. In: *Computer graphics forum*. vol. 40, Wiley Online Library; 2021, p. 633–57.
- [62] Portioli FP. Rigid block modelling of historic masonry structures using mathematical programming: a unified formulation for non-linear time history, static pushover and limit equilibrium analysis. *Bull Earthq Eng* 2020;18(1):211–39.

- [63] Portioli FP, Godio M, Calderini C, Lourenço PB. A variational rigid-block modeling approach to nonlinear elastic and kinematic analysis of failure mechanisms in historic masonry structures subjected to lateral loads. *Earthq Eng Struct Dyn* 2021;50(12):3332–54.
- [64] Iannuzzo A, Van Mele T, Block P. Piecewise rigid displacement (PRD) method: a limit analysis-based approach to detect mechanisms and internal forces through two dual energy criteria. *Mech Res Commun* 2020;107:103557.
- [65] Iannuzzo A, Block P, Angelillo M, Gesualdo A. A continuous energy-based numerical approach to predict fracture mechanisms in masonry structures: CDF method. *Comput Struct* 2021;257:106645.
- [66] Weißenfels C, Wriggers P. Methods to project plasticity models onto the contact surface applied to soil structure interactions. *Comput Geotech* 2015;65:187–98.
- [67] Omata T, Nagata K. Rigid body analysis of the indeterminate grasp force in power grasps. *IEEE Trans Robot Autom* 2000;16(1):46–54.
- [68] Moreau JJ. Quadratic programming in mechanics: dynamics of one-sided constraints. *SIAM J Control* 1966;4(1):153–8.
- [69] Pellegrino S. Structural computations with the singular value decomposition of the equilibrium matrix. *Int J Solids Struct* 1993;30(21):3025–35.
- [70] Portioli F, Casapulla C, Gilbert M, Cascini L. Limit analysis of 3D masonry block structures with non-associative frictional joints using cone programming. *Comput Struct* 2014;143:108–21.
- [71] Cascini L, Gagliardo R, Portioli F. LiABlock_3D: a software tool for collapse mechanism analysis of historic masonry structures. *Int J Archit Herit* 2018.
- [72] Ferris M, Tin-Loi F. Limit analysis of frictional block assemblies as a mathematical program with complementarity constraints. *Int J Mech Sci* 2001;43(1):209–24.
- [73] COMPAS assembly. 2018, URL https://blockresearchgroup.github.io/compas_assembly.
- [74] Hart WE, Laird CD, Watson J-P, Woodruff DL, Hackebeil GA, Nicholson BL, Sirola JD, et al. *Pyomo-optimization modeling in python*. vol. 67, Springer; 2017.
- [75] Wächter A, Biegler LT. On the implementation of an interior-point filter line-search algorithm for large-scale nonlinear programming. *Math Program* 2006;106(1):25–57.
- [76] Mele TV, Liew A, Echenagucia TM, Rippmann M, et al. compas: A framework for computational research in architecture and structures. 2017, <http://compas-dev.github.io/compas/>.
- [77] SOFiSTiK A. SOFiSTiK analysis programs version 2012. 2012, Oberschleißheim: SOFiSTiK AG.
- [78] DeJong MJ, De Lorenzis L, Adams S, Ochsendorf JA. Rocking stability of masonry arches in seismic regions. *Earthq Spectra* 2008;24(4):847–65.
- [79] Atar T, McCabe T, Erdogmus E, Pulatsu B. Dynamic analysis of semi-circular dry-joint masonry arches: Small-scale experiment and discrete element modeling. *Wseas Trans Comput* 2020;19(19):137–42.
- [80] Huerta S. Galileo was wrong: the geometrical design of masonry arches. *Nexus Netw J* 2006;8(2):25–52.
- [81] Blasi C, Foraboschi P. Analytical approach to collapse mechanisms of circular masonry arch. *J Struct Eng* 1994;120(8):2288–309.
- [82] Heyman J. The safety of masonry arches. *Int J Mech Sci* 1969;11(4):363–85.
- [83] Oppenheim IJ. The masonry arch as a four-link mechanism under base motion. *Earthq Eng Struct Dyn* 1992;21(11):1005–17.
- [84] Como M. *Statics of historic masonry constructions*. vol. 1, Springer; 2013.
- [85] Block P, Van Mele T, Liew A, DeJong M, Escobedo D, Ochsendorf JA. Structural design, fabrication and construction of the Armadillo vault. *Struct Eng J Inst Struct Eng* 2018;96(5):10–20.
- [86] Block P, Rippmann M, Van Mele T, Escobedo D. The Armadillo Vault: Balancing computation and traditional craft. *Fabricate* 2017;286–93.